



**HAL**  
open science

## Influence of dissolution on long-term frictional properties of carbonate fault gouge

Hadrien Rattiez, F. Disidoro, Jean Sulem, Manolis Veveakis

### ► To cite this version:

Hadrien Rattiez, F. Disidoro, Jean Sulem, Manolis Veveakis. Influence of dissolution on long-term frictional properties of carbonate fault gouge. *Geomechanics for Energy and the Environment*, In press, pp.100234. 10.1016/j.gete.2021.100234 . hal-03120086

**HAL Id: hal-03120086**

**<https://hal.science/hal-03120086v1>**

Submitted on 25 Jan 2021

**HAL** is a multi-disciplinary open access archive for the deposit and dissemination of scientific research documents, whether they are published or not. The documents may come from teaching and research institutions in France or abroad, or from public or private research centers.

L'archive ouverte pluridisciplinaire **HAL**, est destinée au dépôt et à la diffusion de documents scientifiques de niveau recherche, publiés ou non, émanant des établissements d'enseignement et de recherche français ou étrangers, des laboratoires publics ou privés.

# 1 Influence of dissolution on long-term frictional properties of carbonate fault gouge

2  
3 H. Rattéz<sup>1,4</sup>, F. Disidoro<sup>2</sup>, J. Sulem<sup>3</sup>, M. Veveakis<sup>1</sup>

4 <sup>1</sup>Duke University, Durham, North Carolina, USA.

5 <sup>2</sup>Politecnico di Torino, Turin, Italy.

6 <sup>3</sup>Laboratoire Navier, Ecole des Ponts ParisTech, UGE, CNRS, Champs-sur-Marne, France.

7 <sup>4</sup>Institute of Mechanics, Materials and Civil Engineering (IMMC), Université Catholique de  
8 Louvain, B-1348 Louvain-la-Neuve, Belgium

9 Corresponding author: Hadrien Rattéz ([hadrien.rattéz@duke.edu](mailto:hadrien.rattéz@duke.edu))

## 10 Key Points:

- 11 • Velocity stepping experiments have been conducted on a synthetic calcite gouge using an  
12 annular shear apparatus to study the effect of the injection of an acid fluid on the long-  
13 term frictional properties of the gouge.
- 14 • The dissolution process affects the particle size distribution of the gouge material and the  
15 roughness of the particles.
- 16 • Experimental results show a decrease toward more negative values of the carbonate  
17 gouge Rate and State parameter (a-b) due to dissolution for experiments performed on  
18 dry specimens, whereas an increase of (a-b) is observed for wet experiments.

## 19 20 Abstract

21 Velocity stepping experiments have been performed on a simulated calcite gouge using an  
22 annular shear apparatus to investigate the effect of dissolution on the frictional properties of a  
23 carbonate fault. The tested material was put in contact with hydrochloric acid at different  
24 concentration in order to provoke grains dissolution prior to the experiments. Particle size  
25 analysis shows that the small grains tend to disappear due to the chemical reaction, whereas the

26 distribution of large grains is not much affected. The dissolution process induces a decrease of  
27 the fractal number of the grain size distribution and an increase of the roughness of the particles.  
28 The study of the rate-and-state parameter of the materials, which is commonly used to  
29 characterize the ability of the fault to generate earthquakes, shows a decrease toward more  
30 negative values with dissolution for dry specimens and an increase for wet samples. Moreover, a  
31 decrease of the steady state friction coefficient is observed with dissolution for wet samples. This  
32 decrease of the friction would promote the triggering of slip along an existing fault after the  
33 injection of an acid fluid like in the cases of CO<sub>2</sub> storage or acid gas disposal projects in a  
34 carbonate reservoir, but the increase of the rate and state parameter (*a-b*) of saturated specimens  
35 implies that the seismogenic potential of faults could potentially be reduced.

### 36 **1. Introduction**

37 A variety of human activities can modify the stress state or the material properties of  
38 underground rocks and, thus, induce potentially a frictional instability at the origin of an  
39 earthquake. Human-induced seismicity has been evidenced for a large range of activities (e.g.,  
40 (Foulger et al. 2018)). Among them, the most commonly reported anthropogenic activities are  
41 mining and water reservoir impoundment, but it can also be caused by hydrofractures, oil and  
42 gas extraction, waste water disposal or geothermal projects (Wilson et al. 2017). Human-made  
43 seismicity have drastically increased in the U.S. since 2001 from a previous average of 21  
44 earthquakes a year to 188 documented in 2011 (Ellsworth 2013). For instance, infrastructures  
45 and people in Oklahoma and southern Kansas face potential damages in the next years from  
46 induced earthquakes, in a similar level to regions known for their large number of natural  
47 earthquakes, like southern California (Schoenball and Ellsworth 2017).

48 Projects like carbon capture and storage, acid gas disposal or enhanced oil recovery involve the  
49 injection of a reacting fluid into a reservoir (Khan, Amin, and Madden 2013). Carbon Capture  
50 and Storage (CCS) is one of the methods considered to reduce emissions of CO<sub>2</sub> into the  
51 atmosphere (Espinoza 2011). The principle is to capture the CO<sub>2</sub> and separate it from other gases  
52 in the combustion smoke of large point sources like cement factories or coal-burning power  
53 plants. Once extracted, the gas is compressed and transported with a pipeline to injection sites for  
54 long term storage. Acid gas disposal is a method used by oil and gas producer to reduce  
55 atmospheric emissions of hydrogen sulphide (H<sub>2</sub>S). A mixture of hydrogen sulphide and carbon

56 dioxide (by-product of ‘sweetening’ sour hydrocarbons) is injected into depleted reservoirs or  
57 deep saline aquifers (Bachu and Gunter 2004). Enhanced oil recovery, also called tertiary  
58 recovery, is a way to improve the extraction of crude oil from reservoir that could not be  
59 extracted otherwise (Rubinstein and Mahani 2015). The most common methods are gas or  
60 chemical injection that modify the viscosity of the oil and improve its mobility. In these cases,  
61 induced seismicity could produce damage to the well or the caprock and deteriorate the sealing  
62 of the reservoirs, leading to the failure of the project.

63 A large number of numerical studies have been devoted to study the mechanisms at the origin of  
64 induced seismicity and to evaluate the maximum magnitude of the earthquake a project may  
65 induce (e.g. Cappa 2012). Most of them consider a hydro-mechanical model and look at the  
66 modifications of the stress state at the location of a known fault in a specific site (Baisch et al.  
67 2010; Yehya, Yang, and Rice 2018; Mortezaei and Vahedifard 2015; Cappa 2012). In these  
68 studies, fluid injection into a reservoir-caprock system bounded by a fault is modelled with  
69 different stress state conditions and assuming various permeability conditions. The stress  
70 modifications induced by the fluid potentially leading to an earthquake can be computed and the  
71 value of the stress drop permits to estimate the magnitude.

72 The injection of an acid fluid does not only change the stress state, but also modifies the  
73 properties of the storage medium and can, in particular, affect the mechanical behavior of fault  
74 zones. Due to the conditions of stresses, temperature and velocity, many complex couplings are  
75 involved in earthquake nucleation and propagation (Rice 2006; Sulem and Famin 2009;  
76 Alevizos, Poulet, and Veveakis 2014; Veveakis, Poulet, and Alevizos 2014; Rattetz and Veveakis  
77 2020). In fault reactivation simulations based on effective stresses modifications, reactivation  
78 through a possible decrease in the frictional strength of fault zones is usually not taken into  
79 account. However, experimental studies have looked at the influence of physico-chemical  
80 interactions on the potential of a fault to create earthquakes (see (Rohmer, Pluymakers, and  
81 Renard 2016) for a review in the context of CO<sub>2</sub> storage). The largest impact of the injection of a  
82 reacting fluid on the mechanical properties has been observed for carbonate reservoirs (Rohmer,  
83 Pluymakers, and Renard 2016), which are potential target formations for CO<sub>2</sub> capture and  
84 storage (Michael et al. 2010). Some experiments have looked at the influence of the short term  
85 effect of the presence of CO<sub>2</sub>-saturated water on the value of the friction coefficient (Samuelson  
86 and Spiers 2012; Anne M H Pluymakers et al. 2014) or the velocity dependence of the friction

87 coefficient (Samuelson and Spiers 2012; Rattetz, Sulem, and Ghabezloo 2014; A. M.H.  
88 Pluymakers, Niemeijer, and Spiers 2016a), which is of primary importance for earthquake  
89 nucleation. To our knowledge, the only experimental study on the long-term effect of a contact  
90 with an acidic fluid is (Bakker 2017) by modifying the gouge content and the fraction of the  
91 different minerals based on chemical calculations.

92 In this work, we perform experiments on analog carbonate fault gouges previously subjected to  
93 different degrees of dissolution at different normal stresses. The aim is to assess the effect of  
94 long-term exposure to an acidic fluid on frictional properties of a carbonate material (section 3).  
95 Carbonate materials are chosen here as many reservoirs and potential sites for injection of CO<sub>2</sub>  
96 storage or acid gas disposal are carbonate formations (Bjorlykke 2010). The mechanical results  
97 obtained from annular shear experiments on dry and wet specimens and microstructural  
98 observations are used to infer the micro-physical processes controlling frictional sliding of  
99 calcite fault gouges and discuss the potential effect of dissolution on fault's reactivation (section  
100 4).

## 101 **2. Experimental setup**

### 102 **2.1. Materials**

103 The material used for the experiments is a carbonate rock powder extracted from the Fergues  
104 quarry by the company "les Carrières du Boulonnais" located in the North of France. The  
105 powder is produced by crushing of rocks from the quarry and is composed of 99% of calcite  
106 (CaCO<sub>3</sub>) and show traces of quartz (SiO<sub>2</sub>), magnesium carbonate (MgCO<sub>3</sub>), Hematite (Fe<sub>2</sub>O<sub>3</sub>)  
107 and Aluminum Oxide (Al<sub>2</sub>O<sub>3</sub>). The grain size distribution is obtained using a combination of  
108 sieves and hydrometer analysis or laser diffraction. Both methods show similar results and the  
109 broad grain size distribution of the material is shown in Figure 1.

110 To study the effect of dissolution, granular samples are placed in a large plastic container with a  
111 certain amount of water and then, a solution of hydrochloric acid (mass concentration of 10%) is  
112 slowly poured. In the meantime, the solution is stirred with an electric mixer to obtain a uniform  
113 dissolution in the sample. Hydrochloric acid is a strong acid and is used here to simulate the  
114 long-term effect of dissolution by a weak acid like carbonic acid on the grain size distribution.  
115 The reason for using this acid, instead of carbonic acid or other acids, corresponding to the fluid  
116 injected in the case of acid gas injection or enhanced oil recovery, is that the kinetics of the

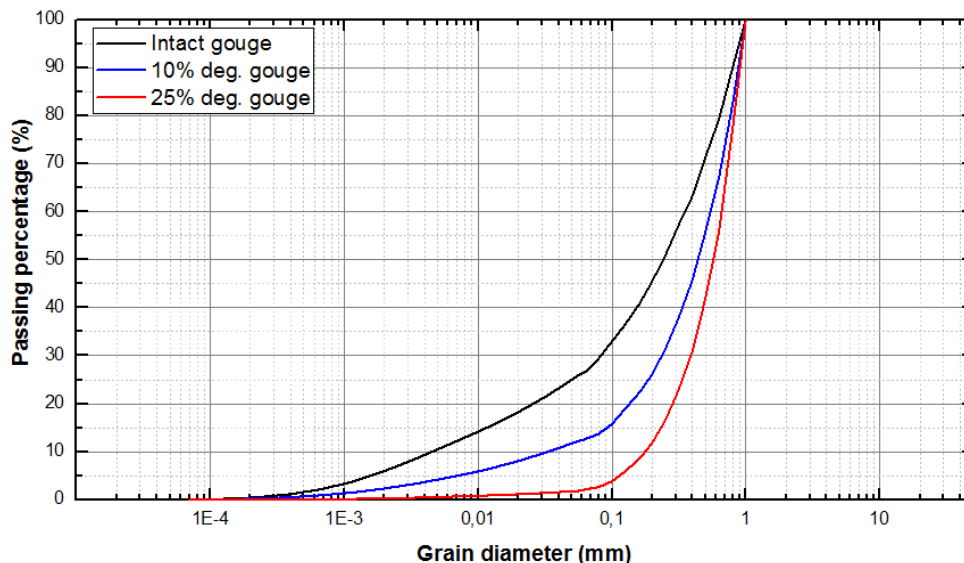
117 chemical reaction is almost instantaneous. The calcium carbonate ( $\text{CaCO}_3$ ) is dissolved by the  
118 hydrochloric acid (HCl) and the products of reaction are carbon dioxide ( $\text{CO}_2$ ), water ( $\text{H}_2\text{O}$ ) and  
119 calcium chloride ( $\text{CaCl}_2$ ) (Lund et al. 1975). The equation of the chemical reaction is:



120  $\text{CaCl}_2$  is highly soluble (Kirk-Othmer 2004) and the specimens put in contact with the acid are  
121 then washed several times with water after the end of the reaction to ensure that this product is  
122 removed. The degrees of degradation chosen for this study are 10% and 25% weight percentages  
123 of material that is dissolved from the acid during the reaction. The software ChemDigiT is used  
124 to calculate the exact quantity of hydrochloric acid required to dissolve the various amounts of  
125 materials. Considering that the software provides the amount of pure hydrochloric acid (no  
126 dilution with water), while the solution at our disposal had a concentration of 23% in weight  
127 (100 g of solution: 23 g of HCl + 77 g of  $\text{H}_2\text{O}$ ), we have scaled the provided quantities as  
128 function of this concentration. The amount of water initially placed in the container with the rock  
129 powder is calculated for the hydrochloric solution to not exceed 10% in weight.

130

131



132

133 *Figure 1. Cumulative grain size distribution of the simulated fault materials showing different level of dissolution*

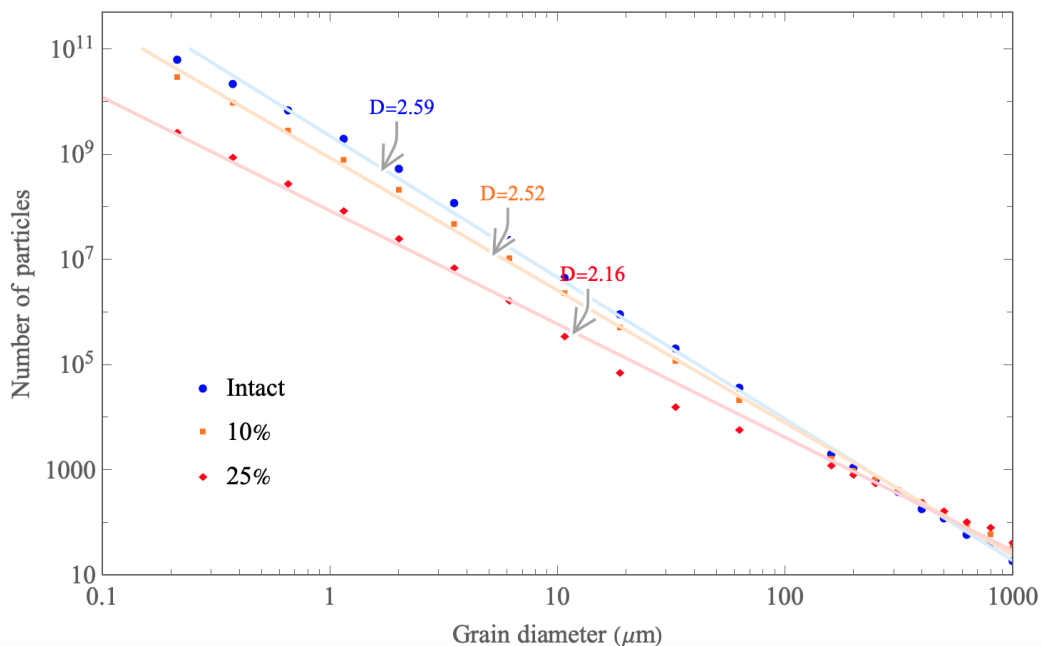
134 The cumulative grain size distributions of the samples for the initial material, after 10% and 25%  
135 of dissolution of the total mass are shown in Figure 1. In particular, the higher the degradation,

136 the more the small particles get dissolved. This phenomenon is due to the greater specific surface  
137 that small particles offer to the reactive fluid compared to bigger particles.

138 Considering that our tests are carried out on a material that is supposed to simulate a natural fault  
139 gouge, one of the most important material properties to be assessed is the fractal dimension of  
140 the grain size distribution. The fractal dimension ( $D$ ) is defined by  
141  $N = r^D$ , where  $N$  is number of particle of diameter  $r$ . (Sammis, King, and Biegel 1987)  
142 measured the particle distribution of intact gouge samples retrieved from the Lopez Fault in the  
143 San Gabriel Mountains of Southern California. The gouge is composed mainly of feldspars,  
144 quartz and chlorite, with smaller amounts of calcite and other oxides. The analysis has revealed a  
145 remarkable degree of self-similarity for the grain size distribution and the authors have found the  
146 fractal dimension to be  $1.60 \pm 0.11$  in two-dimensional cross-section. Thus, the fractal dimension  
147 is  $2.60 \pm 0.11$  in a three-dimensional volume as a general result of fractal theory states that the  
148 fractal dimension of an isotropic three-dimensional figure is greater by unity than a two-  
149 dimensional cross-section of it (Sammis, King, and Biegel 1987). On the basis of the  
150 observations, they proposed a new model, called the comminution model, for the mechanical  
151 processes that generate fault gouges. Self-similarity results from repeated tensile splitting of  
152 grains and that splitting probability depends largely on the relative size of nearest neighbors:  
153 during the fragmentation process, the direct contact between two particles of near equal size will  
154 result in the tensile breakup of one of the two. In this way, at the end of fragmentation process,  
155 the material will have a particle distribution in which particles of the same size are separated  
156 from each other. Such a spatial organization repeats itself at each scale, providing a self-similar  
157 grain size distribution having a fractal dimension of 2.58, independently of the initial size  
158 distribution of the particles. After the development of this model, several authors conducted  
159 experiments on natural and simulated fault gouges, showing their tendency to develop a fractal  
160 dimension values of about 2.6 supporting the Sammis' theory (Steacy and Sammis 1991; An and  
161 Sammis 1994). Moreover, (Biegel, Sammis, and Dieterich 1989) have investigated the frictional  
162 properties of gouge presenting fractal dimension of 2.6 and in particular the role of the minimum  
163 and maximum grain size. However, (Storti, Billi, and Salvini 2003) have analyzed gouge  
164 samples of a carbonate fault in the Apennines, Italy and have shown that for this material the  
165 comminution model is not always verified. Fractal dimensions obtained from fault cores varies  
166 from 2.61 to 3.49 in strike-slip faults' gouge and between 2.17 to 2.74 in the breccia zones. They

167 recognized the value 2.6 to be a threshold between a first stage of fault gouge formation  
168 dominated by particles fragmentation and a second one dominated by particles abrasion in the  
169 case of carbonate materials.

170 In Figure 2, the number of particles as a function of the grain diameter is shown for the different  
171 level of dissolution of the grains. The value of the fractal number of the simulated gouge that is  
172 not dissolved (intact) is in agreement with the comminution theory and this material can,  
173 therefore, be considered as a good analog of a gouge material at the first stage of formation. The  
174 dissolution induces a decrease of the fractal number from 2.59 to 2.16. This decrease is due to  
175 the preferential dissolution of the small particles from the grain size distribution, in the same way  
176 that abrasion makes the fractal number increase due to the creation of more small particles. An  
177 interesting feature of the effect of dissolution on the particle size distribution is that it induces an  
178 increase of the mean grain diameter. It can, thus, affect the prediction of continuum models  
179 considering the mean grain size explicitly into the constitutive laws. These class of models are  
180 used in particular to regularize the problem of strain localization like Cosserat continua (Rattez,  
181 Stefanou, Veveakis, et al. 2018).



182

183 *Figure 2. Number of particles as function of the grain diameter for different level of dissolution of the carbonate rock powder.*  
184 *The points represent the experimental data obtained from sieve and hydrometer analyses. The lines represent an interpolation of*  
185 *the experimental data using a power law. The fractal number associated  $D$  with each distribution is also shown.*

## 186 2.2.Experimental set-up

187 The device used for the mechanical tests is an annular simple shear device called ACSA  
188 (“Appareil de Cisaillement Simple Annulaire”), designed in 1993 in the CERMES laboratory of  
189 Ecole des Ponts (Unterreiner et al. 1993). It has been used in the context of fault mechanics by  
190 (Guillaume Chambon, Schmittbuhl, and Corfdir 2006a, 2006b; Messen, Corfdir, and  
191 Schmittbuhl 2013). This device enables to shear the gouge material over large displacements and  
192 with samples that are thicker than other experimental devices. This thickness of the samples  
193 (10cm) represents an average value of the fault core thickness measured on outcrops of carbonate  
194 rocks (Billi 2005; Torabi, Johannessen, and Ellingsen 2019). A schematic view of the machine is  
195 shown in Figure 3. We only present here this apparatus briefly. A more detailed description can  
196 be obtained from (Guillaume Chambon 2003; Corfdir, Lerat, and Vardoulakis 2004).

197 The internal surface of a ring-shaped sample, which presents a square section of  $100 \times 100 \text{ mm}^2$ , is  
198 sheared by the rotation of a rough steel cylinder. A 15-bit optoelectronic rotation encoder is used  
199 to monitor the rotation angle  $\phi$  of the steel cylinder providing a  $0.011^\circ$  resolution. The tangential  
200 displacement  $\delta$  at the inner boundary of the sample is deducted as  $\delta = \phi \cdot R_i$  (where  $R_i$  is the inner  
201 radius of the sample) and is measured with a resolution of  $1.92 \cdot 10^{-5} \text{ m}$ . The spacing between the  
202 vertical triangular striation of the inner interface is 1mm, the same size as the maximum grain  
203 diameter of the samples, in order to preclude interfacial slip along the steel-granular boundary  
204 (Koval et al. 2011). The outer boundary of the sample is subjected to a constant radial  
205 confinement  $\sigma_e$  through a 1.5-mm-thick neoprene jacket and applied using water by a pressure-  
206 volume controller (max. press: 2 MPa, vol.:  $10^{-3} \text{ m}^3$ , resolution: 1 kPa and  $1 \text{ mm}^3$ , accuracy  
207  $< 0.25$  per cent). Vertically, the sample is embedded between an upper plate made of duralumin  
208 and a lower plate made of glass.

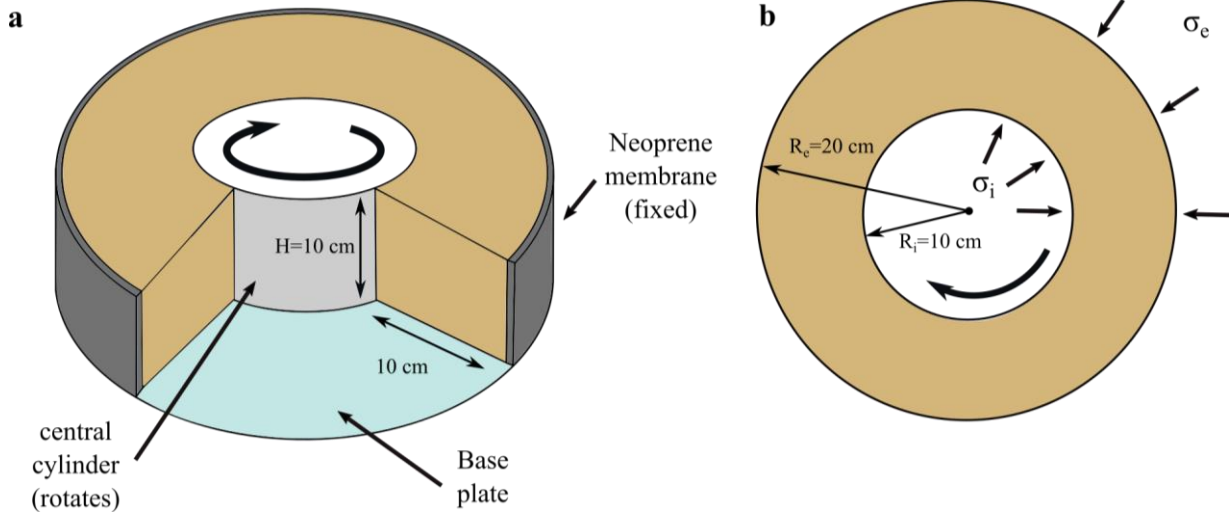


Figure 3. Schematic view of ACSA: a, Cut away view, b, top view

209

210

211 For a given normal stress, the samples are initially sheared at a constant speed of  $33 \mu\text{m/s}$  for 10  
 212 cm, in order to reach the steady-state friction coefficient. Then, the shearing velocity is  
 213 instantaneously changed every 2 mm of slip to apply different velocity steps. The sequence  
 214 shown in Table 1 is chosen such that each velocity step is repeated at least twice to better  
 215 constrain the value of the friction parameters calculated. At the end of this phase, the shear force  
 216 is unloaded, normal stress is increased and the procedure is repeated as in (Scuderi et al. 2013;  
 217 Berend A. Verberne et al. 2015). It should be noted that the different normal stresses applied on  
 218 the sample in this case also correspond to different applied displacements to the sample, which  
 219 could affect the mechanical behavior.

Stage	1	2	3	4	5	6	7	8	9
Displacement [mm]	100	2	2	2	2	2	2	2	2
Speed [ $\mu\text{m/s}$ ]	33	10	1.7	10	33	10	1.7	10	33

220

Table 1. Velocity stepping sequence applied to the sample for a given normal stress.

221 In Table 2, a list of all the conducted tests with different degrees of dissolution, different stages  
 222 consisting of various normal stresses and conditions of saturation is presented. The “dry”  
 223 experiments have been conducted in nominally dry conditions, that is with room atmosphere  
 224 inside the pore space, while the “wet” experiments are conducted on specimens that are saturated  
 225 with deaerated water and tested in drained conditions. We note that the samples were saturated in  
 226 two steps: the water was first injected from the bottom of the specimen until the water level  
 227 reached the valves located at the top, then the flow through the specimen was maintained until

228 half the total volume of pore space of the specimen was expelled at the top, to ensure conditions  
 229 close to homogeneous saturation.

Degradation	$\sigma_i$ (MPa)	saturation	Set of data name
none	0.6	dry	Intact0.6
none	1	dry	Intact1
none	1.6	dry	Intact1.6
10%	0.6	dry	10deg0.6
10%	1	dry	10deg1
10%	1.6	dry	10deg1.6
25%	0.6	dry	25deg0.6
25%	1	dry	25deg1
none	0.6	wet	Intact0.6w
none	1	wet	Intact1w
none	1.6	wet	Intact1.6w
10%	0.6	wet	10deg0.6w
10%	1	wet	10deg1w
10%	1.6	wet	10deg1.6w
25%	0.6	wet	25deg0.6w
25%	1	wet	25deg1w
25%	1.6	wet	25deg1.6w

Table 2 – List of complete set of phases and experiments

230

### 231 2.3. Data acquisition and processing

232 The apparent friction coefficient  $\mu$  of the sample is calculated as the ratio of the applied shear  
 233 stress  $\tau$  to the normal stress  $\sigma$ ,  $\mu = \frac{\tau}{\sigma}$ . The shear stress  $\tau$  can be found converting the applied  
 234 torque measurements  $\Gamma$ , measured by a torquemeter of 20 N.m accuracy:

$$\tau = \frac{\Gamma/r}{2\pi rH} = \frac{\Gamma}{2\pi r^2H} \quad \#(1)$$

235 where  $r$  and  $H$  are respectively the radius and the height of the inner cylinder and are both equal  
 236 to 10 cm. The normal stress exerted on the inner cylinder is different from the external normal  
 237 stress applied on the outer boundary of the sample due to the particular geometry of the sample.  
 238 According to (Guillaume Chambon 2003), simple geometrical considerations indicate that the  
 239 inner normal stress  $\sigma_i$  should be equal to twice the applied confinement  $\sigma_e$ , since the external  
 240 radius of the sample is the double of the internal one; moreover, the same authors conducted  
 241 some experiments equipping both the smooth and the rough cylinder with five stress sensors, and

242 they found that normal stress on cylinders' surface was strongly varying at the beginning of the  
 243 test, but it tended to stabilize after few millimeters of slip toward values very close to the double  
 244 of external pressure. As the shear band is developing near the inner cylinder, the apparent  
 245 friction is calculated as:

$$\mu = \frac{\tau}{\sigma_i} = \frac{\Gamma}{2\pi r^2 H} \cdot \frac{1}{2\sigma_e} \#(2)$$

#### 246 **2.4.The Rate-and-State Friction (RSF) law**

247 (Reid 1910) was the first to argue after the 1906 San Francisco earthquake that this phenomenon  
 248 is not created by the emergence of a new crack in the crust, but rather by the sudden slip along an  
 249 existing fault. After the beginning of slipping the fault can move aseismically or seismically  
 250 (Scholz 1998) if a frictional instability is triggered. An empirical law describing the instability  
 251 along a fault was developed during the eighties by Dieterich and Ruina (Dieterich 1981; Ruina  
 252 1983). They introduced new state variables that describe a second order effect on the coefficient  
 253 of friction. These laws are called "Rate and State", because the friction depends on the velocity  
 254 of slipping (Rate) and a state variable  $\theta$ , which is interpreted as the average lifespan of a set of  
 255 grain-to-grain contacts in a frictional system. They describe the evolution of the friction  
 256 coefficient to changes in sliding motions by the equation:

$$\mu = \mu_0 + a \ln\left(\frac{V}{V_0}\right) + b \ln\left(\frac{V_0 \theta}{D_c}\right) \#(3)$$

257  $\mu_0$  is a reference friction coefficient,  $V$  and  $V_0$  are respectively the actual and reference velocities  
 258 of the fault.  $D_c$  is the critical slip distance representing the slip necessary to renew contacts,  
 259 associated with the state variable  $\theta$  (Marone 1998).  $a$  and  $b$  are empirical parameters. The  
 260 observed evolution of the state variable can be described by the following equation (Dieterich  
 261 1979):

$$\frac{d\theta}{dt} = 1 - \frac{v\theta}{D_c} \#(4)$$

262 These empirical laws can capture the repetitive stick-slip failure at the origin of the seismic  
 263 cycle. A simple system called the spring-slider model, in which the slider follows the rate and  
 264 state friction laws and the spring represents the elastic surrounding mass of the fault, is usually  
 265 applied to model seismic slips. The study of the linear stability of that system (Rice and Ruina

266 1983) shows a critical value for the stiffness of the spring  $k_{cr}$  (if the inertial terms are  
267 negligible). Under this value, the system is unstable and over this value, it is conditionally stable.

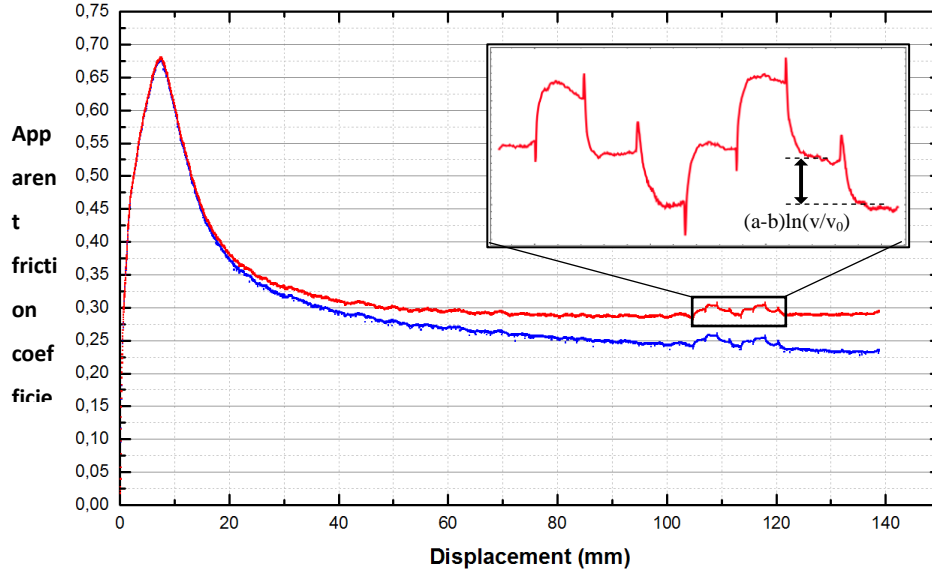
$$k_{cr} = \frac{\sigma_N}{D_c}(b - a) \#(5)$$

268 where  $\sigma_N$  is the effective normal stress applied perpendicular to the direction of sliding.  
269 The parameter  $(a - b)$  is therefore fundamental to determine the stability of a fault modelled  
270 with a rate and state friction law, because if it is positive, frictional instability would not nucleate  
271 with this model. Moreover, a modification of the value of  $(a-b)$  in the velocity-weakening regime  
272 modifies the value of the critical stiffness and, if  $(a-b)$  becomes more negative (stronger  
273 weakening), it can lead to seismic slips for faults that were stable before the modification.

274 The parameter  $(a - b)$  can be calculated based on the values of the steady-state friction before  
275 and after an instantaneous velocity change. At steady-state ( $d\theta/dt = 0$ ) and the state evolution  
276 law gives  $\theta = D_c/v$ . So, equation (3) becomes:

$$\mu = \mu_0 + (a - b)\ln \frac{v}{v_0} \#(6)$$

277 To evaluate the friction parameter  $(a-b)$ , the general long-term strain trend of the apparent  
278 friction is removed in order to avoid this factor to influence the  $(a-b)$  values. It is typically a  
279 softening trend as the one shown in Figure 4. The same procedure was also applied by several  
280 studies (Blanpied, Lockner, and Byerlee 1995; Tembe, Lockner, and Wong 2010; Samuelson and  
281 Spiers 2012) for velocity stepping experiments.



282

283

Figure 4. Apparent friction coefficient evolution with displacement: original (blue) vs detrended (red) (intact0.6).

284

The  $(a-b)$  value of each velocity step can be obtained from the detrended evolution of the friction coefficient, and in particular, from the value of residual friction before the velocity change and the one obtained once a new steady state is obtained after the change:

285

286

$$(a - b) = \frac{\mu_0 - \mu}{\ln(V/V_0)} \#(7)$$

287

where  $\mu$  is the coefficient of friction at the end of a step with velocity  $V$ , and  $\mu_0$  and  $V_0$  are the coefficient of friction and velocity immediately prior to the velocity step.

288

289

### 3. Results

290

In this section, we describe first the frictional data obtained from the mechanical experiments.

291

The global evolution of the apparent friction as well as the rate and state parameter  $(a-b)$  are

292

presented together with their evolution with normal stress and dissolution rate. Secondly, the

293

specific surface areas of the samples are assessed by two methods in order to estimate the

294

rugosity of the grains. This analysis is completed with observations obtained using a scanning

295

electron microscope to interpret the different mechanical responses of the samples.

296

#### 3.1. Mechanical results

297

An example of the apparent friction coefficient evolution with shear displacement is shown in

298

Figure 4. It exhibits a peak for a value between 0.6 and 0.7 for all dry experiments at 600 kPa of

299

imposed normal stress. The peak is more pronounced for a normal stress of 600 kPa as it is the

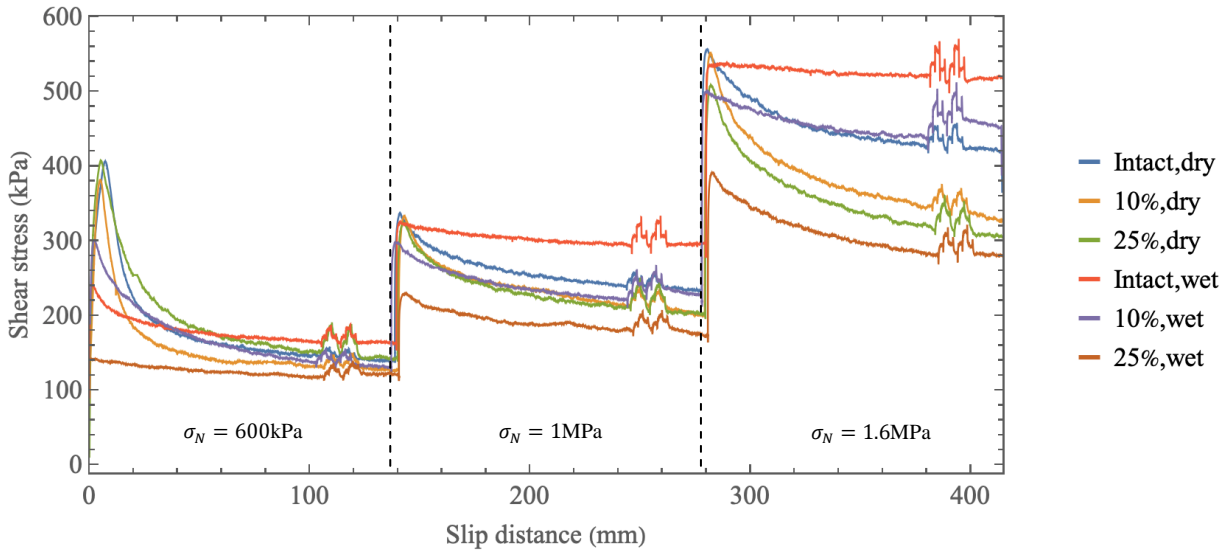
300 first run applied to the material. This peak is followed by a slip-weakening behavior with a  
301 characteristic slip distance of a few centimeters, also observed in the experiments performed on  
302 glass beads and quartz sand by (Guillaume Chambon, Schmittbuhl, and Corfdir 2006a). The  
303 evolution of the shear stress for all the stages of the experiments is shown in Figure 5 for the  
304 different samples. The peak stress is less important for the normal stresses 1 and 1.6 MPa than  
305 for 600 kPa due to the multi-stage procedure.

306 We observe through the glass window at the bottom of the sample a strain localization of the  
307 deformation next to the inner cylinders. The shear band thickness is on the order of a few  
308 millimeters, which corresponds approximately to 10 times the mean grain size, in accordance  
309 with results of numerical simulations of continuum models of granular media (Rattez, Stefanou,  
310 Sulem, et al. 2018; Rattez, Stefanou, and Sulem 2018). However, digital image correlation needs  
311 to be used to observe accurately the evolution of the thickness with increasing displacements as  
312 in (G. Chambon et al. 2003) but has not been carried out for this study.

313 The value of the friction  $\mu$  is not much affected by the dissolution in the dry case (see Figure 5  
314 and Table 3), except for the residual friction at 1.6 MPa of normal stress. We can see that for the  
315 tests performed under 600 kPa of normal stress, the three peak values are nearly the same  
316 ( $\mu=0.63-0.67$ ), as well as the residual values ( $\mu=0.22-0.25$ ). The same happens in the tests under  
317 1 MPa of normal stress where the peak is exactly the same and the intact residual value is only a  
318 bit higher than the degraded ones ( $\mu=0.20$ ). Finally, the 1.6 MPa run exhibits only a difference in  
319 the value of the residual friction. In the wet experiments, the peak values and the residual friction  
320 coefficients show a decrease with the dissolution (except the peak stress between the intact and  
321 deg10 for the 600 kPa, which can be due to different degrees of initial compaction) for all normal  
322 stresses. For the wet experiments, the residual friction decreases from  $\mu=0.27-0.33$  for the intact  
323 gouge to  $\mu=0.14-0.15$  for the gouge dissolved at 25%.

324 Regarding the velocity stepping experiments, the results presented in Figure 6 and Figure 7 show  
325 that all of the tests performed in this study, regardless of degradation level and pressure, exhibit a  
326 velocity weakening behavior. The  $(a-b)$  values are falling between -0.003 and -0.018; the only  
327 exception is the 25deg0.6dry test (see Table 2 for the denomination of the tests), which exhibits a  
328 more negative value of  $(a-b)$  reaching -0.028.

329 For dry samples, we can see that deg10 results are situated between intact and deg25 ones (see  
 330 Figure 6 a, c, e). It means that a larger amount of degradation induces a more pronounced  
 331 velocity-weakening, and this trend is clear for the tests at 0.6, 1 MPa of normal stress and the  
 332 velocity steps 10-33  $\mu\text{m/s}$  at 1.6 MPa, but is not visible for the velocity steps 1.7-10  $\mu\text{m/s}$  at 1.6  
 333 MPa. For the wet experiments, the opposite effect is observed (see Figure 6 b, d, f), the  
 334 dissolution of the grains leads to coefficients (a-b) that are less negative, even though we still  
 335 observe a velocity weakening.



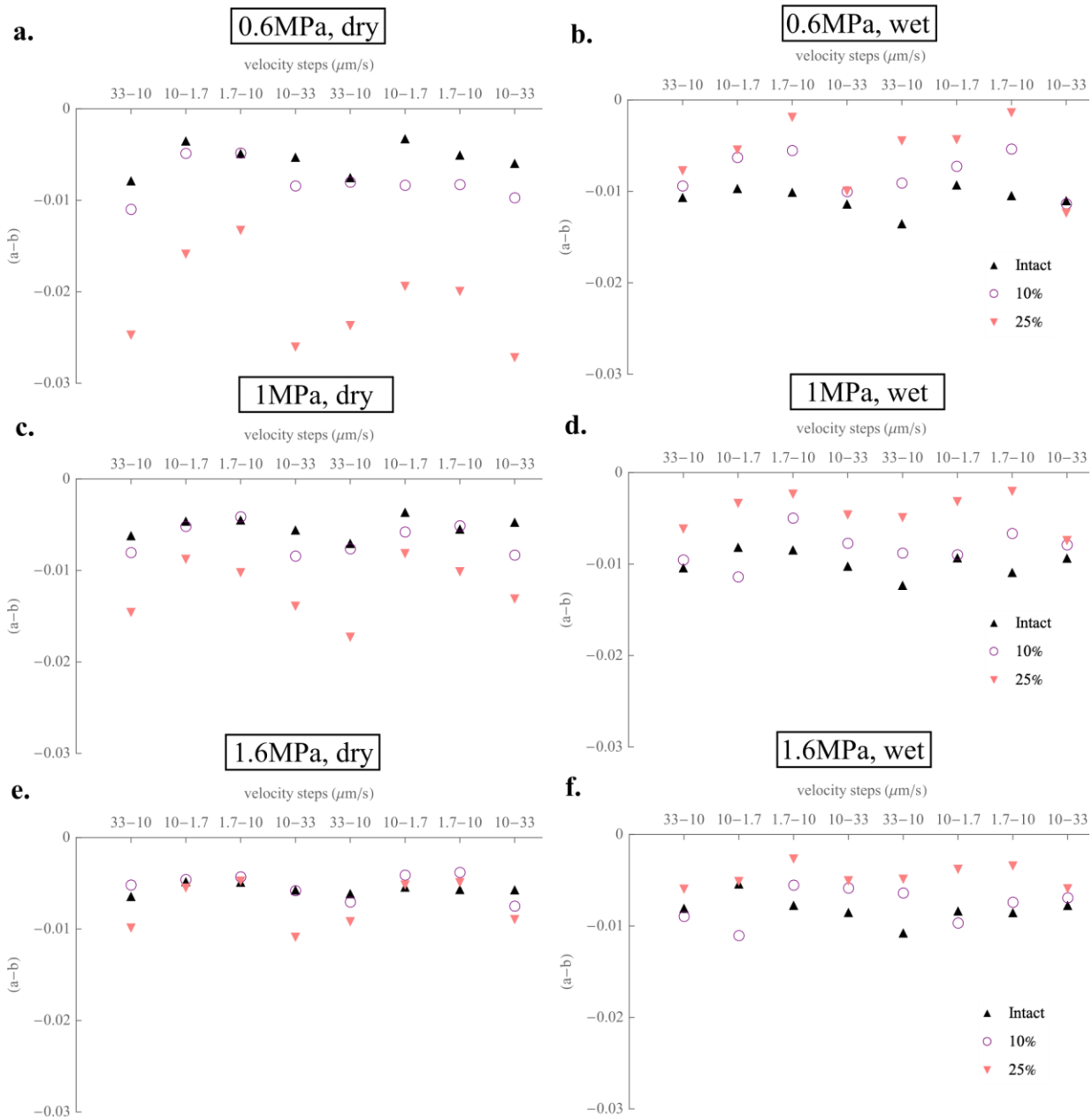
336  
 337  
 338  
 339  
 340  
 341

Figure 5. Shear stress as a function of the displacement of the inner cylinder for the different experiments

	0.6 MPa		1 MPa		1.6 MPa	
	peak	residual	peak	residual	peak	residual
<b>intact</b>	0.67	0.24	0.34	0.24	0.35	0.26
<b>dissolution 10%</b>	0.67	0.21	0.33	0.20	0.34	0.21
<b>dissolution 25%</b>	0.64	0.24	0.32	0.20	0.32	0.19
<b>Intact, wet</b>	0.4	0.27	0.33	0.30	0.33	0.33
<b>dissolution 10%, wet</b>	0.5	0.22	0.3	0.23	0.31	0.29
<b>dissolution 25%, wet</b>	0.24	0.15	0.23	0.14	0.24	0.14

342 Table 3. Values of the residual apparent friction coefficient for different normal stresses and level of dissolution

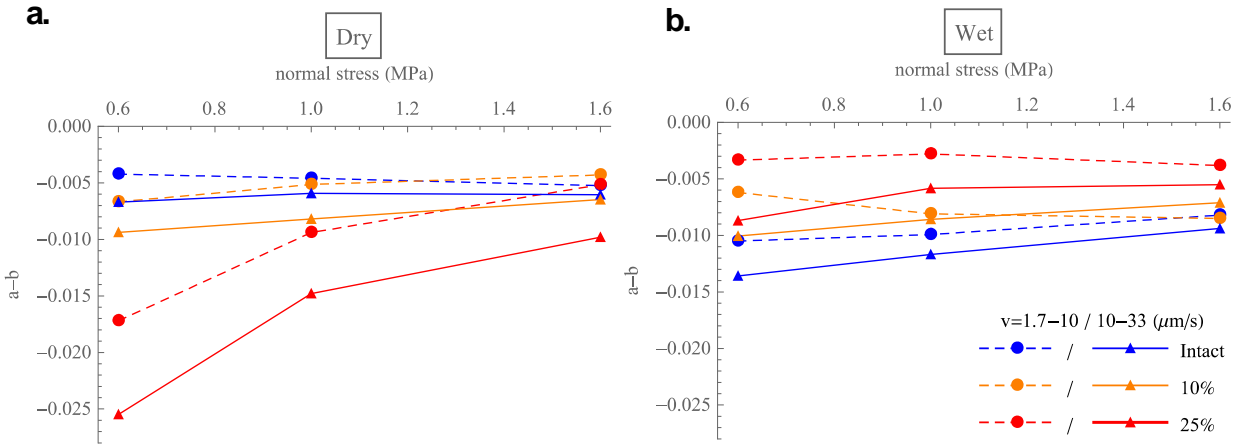
343 In Figure 7, the values of the friction parameters ( $a-b$ ) are plotted as a function of the normal  
344 stress for the different degrees of dissolution and velocity steps. The different values obtained for  
345 a velocity step are calculated as an average of the values of the velocity jumps involving the  
346 same velocity values (velocity jump 10-33  $\mu\text{m/s}$ : 1-2, 4-5, 5-6, 8-9; velocity jump 1.7-10  $\mu\text{m/s}$ :  
347 2-3, 3-4, 6-7, 7-8). For the intact gouge, the rate and state parameter ( $a-b$ ) increase slightly with  
348 the normal stress but a more visible dependency on the velocity steps considered is observed.  
349 The transition from 10 to 33  $\mu\text{m/s}$  induces more weakening than the transition from 1.7 to 10  
350  $\mu\text{m/s}$ . This effect is also observed for the degraded gouge. The dry gouges that underwent 10%  
351 and 25% dissolution show a distinct increase of the rate and state parameter ( $a-b$ ) with the  
352 normal stress (more pronounced for 25% dissolution). In these tests, the ( $a-b$ ) values get closer to  
353 zero when the confinement pressure is increased. For the intact sample, ( $a-b$ ) shows no clear  
354 variation with the normal stress. For the wet samples, we also observe a slight increase of ( $a-b$ )  
355 with the normal stress for the intact sample. However, for the samples with 10 and 25%  
356 degradation, this increase is only observed for the velocity step 10-33  $\mu\text{m/s}$  and no clear trend is  
357 observed for the velocity step 1.7-10  $\mu\text{m/s}$ . It should be noted that the different normal stresses  
358 applied here correspond also to larger displacements due to the multi-stage applied to the  
359 material, which could affect the evolution of ( $a-b$ ) observed here.



360

361  
362

Figure 6. Effect of the dissolution on the rate and state friction parameters (a-b) for the different velocity steps and for different normal stress.



363

364  
365

Figure 7. Effect of the normal stress on the rate and state friction parameters (a-b) plotted for the different velocity steps and for different rate of dissolution

366

### 3.2. Roughness of the grains

367

The dissolution of the calcite through contact with an acid solution before shearing affects not only the grain size distribution but also the shape of the particles. The shape and in particular the roughness of the grains could influence the mechanical response of the sample (Anthony and Marone 2005). Thus, we characterize the roughness and shape of the particles using the specific BET surface area (SA 3100 BET surface area and pore size analyzer; Beckman Coulter, U.S.), sieves analysis and a Scanning Electron Microscope (SEM).

373

The roughness of a given sample is defined as the ratio between the surface areas obtained from the BET method and the particle size analysis (considering spherical particles) as explained in (Micić et al. 2017). The BET method is a way to calculate the specific surface area of a sample based on gas adsorption. Nitrogen is pumped into the sample at a given pressure, with constant temperature (corresponding to the boiling point of liquid Nitrogen) and the adsorption process is measured volumetrically. The isotherm data obtained from this procedure enable to determine the specific surface area based on the theory developed by (Brunauer, Emmett, and Teller 1938) with an accuracy of  $0.1 \text{ m}^2/\text{g}$ . This value of the specific surface area can be compared with one obtained from the particle size distribution (PSD). The latter is obtained by assuming that the mass of material obtained for each size correspond to spherical particles with the diameter of the mesh size (or the size of the volume equivalent for laser diffraction). The results are reported in Table 4.

384

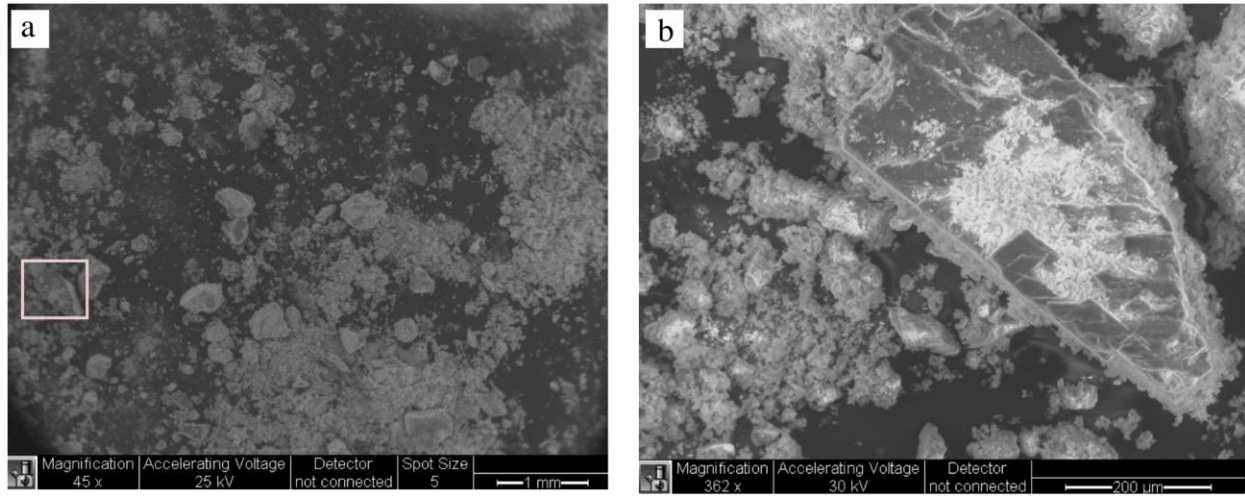
<b>Sample</b>	<b>S<sub>PSD</sub> (m<sup>2</sup>/g)</b>	<b>S<sub>BET</sub> (m<sup>2</sup>/g)</b>	<b>Roughness</b>
<b>Intact</b>	5.34×10 <sup>-2</sup>	0.96	18.03
<b>10%</b>	3.29×10 <sup>-2</sup>	0.83	25.32
<b>25%</b>	9.48×10 <sup>-3</sup>	0.99	104.32

386 *Table 4. Values of the specific surface area obtained from the BET method (S<sub>BET</sub>) or the particle size distribution (S<sub>PSD</sub>) and the*  
387 *roughness for different level of dissolution*

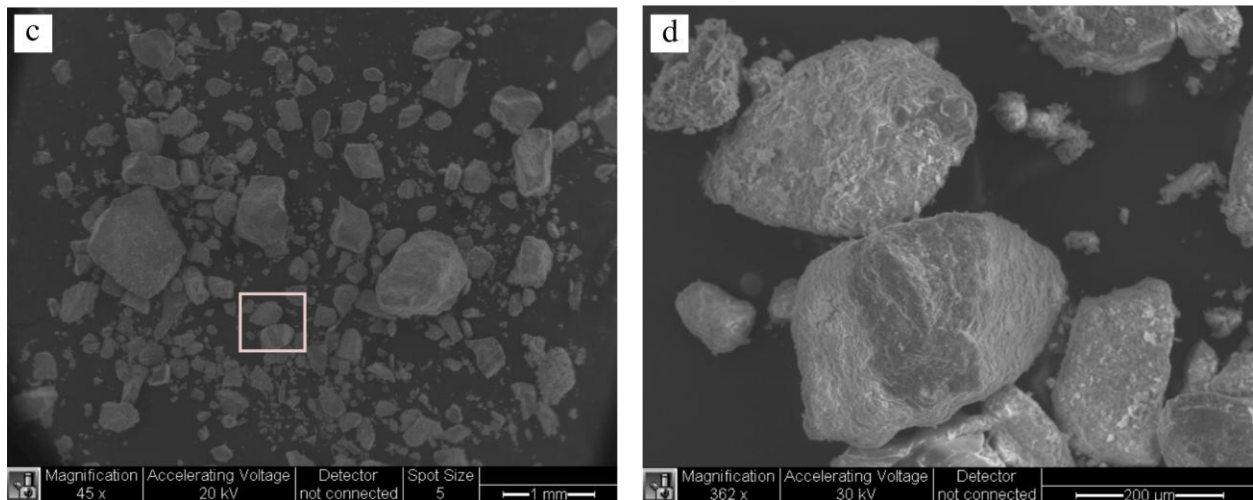
388

389 The specific surface area obtained from the PSD exhibits a decrease with the amount of  
390 dissolution. It is due to the more pronounced dissolution of the small particles that contributes  
391 substantially to the value of the specific surface. However, the values obtained from the BET  
392 method are not notably affected by the dissolution. Consequently, the roughness increases with  
393 the increasing amount of dissolution. (Micić et al. 2017) have performed a similar methodology  
394 to evaluate the roughness of different granular materials. They have observed a difference of  
395 almost two orders of magnitude for the same definition of the roughness used here between glass  
396 beads with a diameter of 1 mm and Dorsilit8 sand composed of 95% of quartz presenting  
397 moderately well-sorted angular grains (0.3–0.8 mm), which shows that the difference of the  
398 values of roughness reported in Table 4 are reasonable. To understand our results, observations  
399 of the grains have been performed using a Variable Pressure Scanning Electron Microscope (FEI  
400 XL30 SEM). The specimens have been coated with gold film prior to be placed in the  
401 microscope. Images of the intact gouge and the gouge with 25% degradation are shown in Figure  
402 8. The intact gouge exhibits much more fine particles attached to each other or to larger grains  
403 than the samples which experienced dissolution. Moreover, grains with a diameter larger than 10  
404 μm in the intact gouge (Figure 8. b) present an external surface that exhibits less asperities than  
405 the one in the dissolved gouge (Figure 8. d).

## Intact sand



## Dissolved sand 25%



407

408 *Figure 8. Scanning Electron Microscope images of the intact gouge (a and b), and the gouge with 25% dissolution (c and d).*

409

410 **4. Discussion**

411 In this section, we integrate the mechanical data from our experiments and microstructural  
 412 investigation of the gouge prior to shear to discuss the role of the normal stress (see (A. M.H.  
 413 Pluymakers, Niemeijer, and Spiers 2016b) for a broader discussion on the effect of this  
 414 parameter), saturation of water and amount of dissolution on the velocity weakening behavior of  
 415 carbonate bearing faults. We also discuss the implications of our results in the context of  
 416 injection of an acidic fluid in a reservoir presenting faults composed of carbonates.

#### 417        **4.1. Comparison with other works**

418        Our results show that the mechanical behavior of simulated carbonate-bearing faults is  
419        modulated by the imposed slip velocity, the normal stress, the amount of chemical dissolution of  
420        the grains and the presence of water inside the pores.

421        A number of experimental studies have focused on the frictional behavior of carbonate materials  
422        (Han et al. 2007; B. a. Verberne et al. 2013; Smith, Nielsen, and Di Toro 2015; Carpenter et al.  
423        2016) under different range of temperature, velocities and normal stress using double direct shear  
424        and rotary shear experiments. They observed a strong resistance and a friction coefficient at the  
425        peak between 0.6 and 0.7, consistent with our observations for a normal stress of 600 kPa and  
426        sub-seismic velocities. The decrease of the peak friction coefficient in the presence of water has  
427        also been previously observed (B. a. Verberne et al. 2013), but the difference was less  
428        pronounced than in our observations for the dissolved samples. Moreover, the steady state  
429        friction coefficients obtained in experiments reported in the literature stay close to the peak value  
430        (at velocities below 1 cm/s), exhibiting thus almost no slip weakening or slip strengthening. This  
431        discrepancy is due to the size of the sample used in the ACSA as explained in (Guillaume  
432        Chambon, Schmittbuhl, and Corfdir 2006a). This macroscopic slip-weakening operating over  
433        centimetric distances is induced by a progressive mechanical decoupling between the interfacial  
434        layer and the bulk of the samples, as shown by image analysis during shearing (G. Chambon et  
435        al. 2003). This characteristic distance of the slip weakening is much larger than in previous  
436        experimental studies and fully consistent with values inferred for large earthquakes (Guillaume  
437        Chambon, Schmittbuhl, and Corfdir 2006b).

438        Experiments conducted on gouge at typical velocities consistent with earthquake nucleation (a  
439        few micrometers per seconds like here) exhibits velocity strengthening (B. A. Verberne et al.  
440        2014) or a velocity neutral (Carpenter et al. 2016) for normal stresses below 20 MPa. The order  
441        of magnitude of the  $(a-b)$  coefficient, we have obtained ( $10^{-2}$ ) is in agreement with previous  
442        studies on friction in gouge materials composed of quartz or carbonates (Biegel, Sammis, and  
443        Dieterich 1989; Carpenter et al. 2016). Nevertheless, our experiments reveal a velocity  
444        weakening behavior. This weakening has also been observed by (Guillaume Chambon 2003) for  
445        monodisperse quartz sand and glass beads using the annular shear apparatus. The difference in  
446        terms of  $(a-b)$  can be explained by the large displacements applied to the gouge in our

447 experiments before the velocity steps compared to experiments performed in double direct shear  
448 or saw cut configurations. Large-displacement experiments using a rotary shear apparatus with  
449 gouge samples have consistently shown a decrease of the friction rate parameter with  
450 displacement and a transition from velocity-strengthening to velocity-weakening (Beeler et al.  
451 1996; Marone 1998).

#### 452 **4.2. Micro-mechanisms affecting the rate and state friction parameters for dry** 453 **experiments**

454 For the range of normal stresses applied to our samples, the mechanical behavior of the dry  
455 gouge is dominated by sliding and rotation of grains, the creation of force chains, cataclasis and  
456 strain localization (Anthony and Marone 2005; Guillaume Chambon, Schmittbuhl, and Corfdir  
457 2006a; B. a. Verberne et al. 2013). We focus in this section on the possible mechanisms driving  
458 the experiments performed for the dry samples and compare with our observations to infer which  
459 ones seem to dominate.

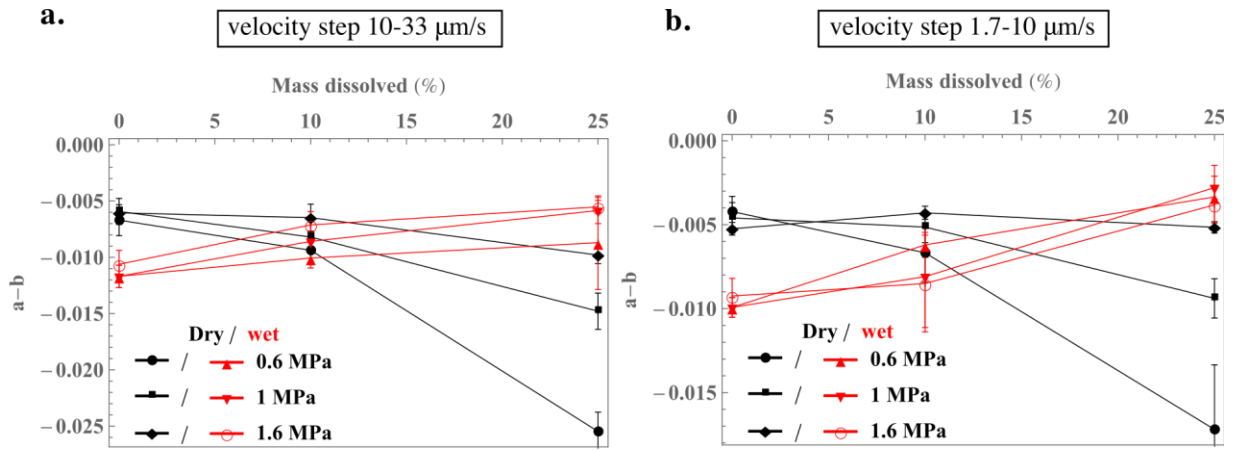
460 The dissolution of the calcite by an acid fluid before shearing affects the samples in two ways.  
461 First, it generates a modification of the particle size distributions by dissolving preferably the  
462 small grains. The fractal number of the distribution decreases and the mean grain size increases.  
463 Moreover, the dissolution modifies the roughness of the particles. Both effects can influence the  
464 frictional behavior of the sample.

465 (Anthony and Marone 2005) have studied the influence of particle roughness on the frictional  
466 behavior of gouge using two materials: spherical glass beads and quartz sand, presenting  
467 comparable particle size distributions. They have shown that an decrease of the  
468 angularity/roughness of the grains for a similar grain size distribution tends to induce a  
469 weakening of the apparent friction coefficient (Anthony and Marone 2005) and the triggering of  
470 stick-slip instabilities (manifestation of a more negative rate and state parameter ( $a-b$ )).  
471 However, our analysis of the roughness of the particles exhibits an increase with the dissolution  
472 but a decrease of the apparent friction (see Figure 5 and Table 4) and a decrease of ( $a-b$ ) towards  
473 more negative values (Figure 6). Therefore, the decrease of the apparent friction and ( $a-b$ ) with  
474 the dissolution for dry experiments cannot be explained as a direct effect of the roughness of the  
475 particles. In the present work, the particle size distribution changes (in addition to the roughness

476 of the grains) when subjected to dissolution, so this effect must dominate the mechanical  
477 behavior of the sample and not the modification of the grains' roughness.

478 Compared to silica sand, carbonate sand presents a lower grain hardness and higher intraparticle  
479 porosity, which makes them more susceptible to grain crushing (Coop et al. 2004). Recent papers  
480 on granular mechanics have linked the rate dependency observed in sand to the crushing of  
481 particles (Karimpour and Lade 2010; Y. D. Zhang and Buscarnera 2017; Das and Das 2019).  
482 This effect induces a larger compaction rate and thus a stronger velocity-weakening behavior as  
483 explained in (Marone 1998). For our experiments, the dissolution affects the width of the particle  
484 size distribution and generates a narrower distribution and a higher fraction of large particle.  
485 Therefore, the force chains between the grains can be expected to carry a higher load and to be  
486 longer (Mair and Hazzard 2007; C. Ovalle et al. 2016). This can lead to a more important  
487 comminution process, a decrease of friction and a larger velocity-weakening (a more negative (*a-*  
488 *b*) parameter) as observed here for the dry experiments in Figure 9 and Figure 5. However, the  
489 fact that we use multi-stage experiments and large displacements before applying the velocity  
490 steps here induces that the velocity steps performed for lower normal stress are performed on a  
491 material that is more subject to grain crushing and a larger compaction rate affecting the values  
492 of (*a-b*) obtained.

493 In Figure 7 and Figure 9, the 25% dry experiments (and also less significantly the 10% dry) show  
494 an increase of the (*a-b*) parameter with the normal stress. The other tests exhibit only a small  
495 variation with the normal stress. This can be attributed to the fact that the experiments with 0.6  
496 MPa normal stress are performed on the initial sample (not yet sheared) and the grains can be  
497 more subject to grain crushing and thus a higher compaction rate, whereas the tests with higher  
498 normal stresses are performed on samples that have already been sheared and thus, the  
499 comminution has already modified the PSD.



500

501 *Figure 9. Comparisons of the average (a-b) parameter obtained for a given velocity jump as a function of the amount of*  
 502 *dissolution for the wet and dry experiments. Error bars indicate the dispersion of the values of (a-b) between the different steps*  
 503 *for the same values of the velocity.*

504 Therefore, the mechanical behavior of the dry experiments is inferred to be mainly caused by the  
 505 grain crushing that is more important for the dissolved samples as the particle size distributions  
 506 become narrower as it allows to explain the evolution observed for the rate and state parameter  
 507 (*a-b*) and the value of the friction coefficient.

### 508 4.3. Effects of water

509 In Figure 9, the values of (*a-b*) for a given step is represented as a function of the percentage of  
 510 mass dissolved by the acid solution for different normal stresses and in presence or not of water.  
 511 The different values obtained for a velocity step are calculated as an average of the values of the  
 512 velocity jumps involving the same velocity values (velocity jump 10-33  $\mu\text{m/s}$ : 1-2, 4-5, 5-6, 8-9;  
 513 velocity jump 1.7-10  $\mu\text{m/s}$ : 2-3, 3-4, 6-7, 7-8). We can observe that the presence of water  
 514 modifies the influence of the dissolution on the coefficient (*a-b*). For dry experiments, the  
 515 dissolution leads to more weakening of the rate parameters towards more negative values,  
 516 whereas in the wet case it leads to an increase of the rate and state parameter (*a-b*). Moreover,  
 517 the addition of water modifies also the value of the friction coefficient at peak and steady state  
 518 compared to the dry experiments (Figure 5). The peak friction is decreased by the presence of  
 519 water compared to the dry experiments, however the steady state friction shows a larger value for  
 520 the intact sample and a lower value in the wet tests compared to the dry tests.

521 As explained in (B. A. Verberne et al. 2014), the effect of unpressurized water is threefold  
 522 regarding the frictional behavior of granular materials. Water can 1) promote compaction of the

523 specimen through pressure-solution; 2) lubricate grain contacts; or 3) stimulate cataclasis by  
524 lowering the fracture toughness of the grains. The influence of these three mechanisms is  
525 discussed in the following paragraphs and compared to our observations to infer which ones  
526 dominate during the experiments presented here.

527 The phenomenon of pressure solution is a time-dependent chemo-mechanical process inducing a  
528 compaction of rocks and granular assemblies when saturated. It is a dissolution-precipitation  
529 mechanism in which the solid is dissolved in stressed regions and precipitates in sheltered  
530 regions relatively under-stressed. This process is more active for fine grain materials (Niemeijer,  
531 Elsworth, and Marone 2009), and would therefore tend to be more active in the intact gouge than  
532 in the dissolved gouges in our case. (X. Zhang and Spiers 2005) performed creep experiments on  
533 calcite with normal stresses between 1 and 4 MPa at room temperature and observed most of the  
534 deformations induced by pressure solution happened within the first few hours of the  
535 experiments. This timescale of pressure solution is similar to the total time of our tests for a  
536 similar material and can therefore influence the mechanical behavior. In particular, pressure  
537 solution during shearing at low velocities leads to a porosity reduction, an increasing grain  
538 contact area (Bos, Peach, and Spiers 2000) and lower absolute value for  $(a-b)$  (more neutral)  
539 (van den Ende et al. 2018). This phenomenon cannot explain the lower value of  $(a-b)$  for in the  
540 wet case compared to the dry for the intact gouge as the slip distances between each velocity  
541 jump is too small for it to develop. However, the increased gouge cohesion due to pressure-  
542 solution in wet experiments should lead to a higher steady-state frictional strength than in dry  
543 tests as observed in Table 3 for the intact and deg10 experiments, which are samples presenting  
544 smaller grains than deg25 and are therefore more subject to pressure solution. It indicates that  
545 this mechanism influences the value of the friction but not the rate and state parameter  $(a-b)$  in  
546 our experiments.

547 The presence of water promotes grain breakage by decreasing the fracture toughness of  
548 individual grains (Atkinson 1982; Carlos Ovalle et al. 2015; Y. Zhang and Buscarnera 2018).  
549 This effect is usually referred as subcritical crack propagation and several theories have been  
550 developed to explain it based on the modification of the plastic zone near the crack tip or  
551 chemical interactions of the water with bonds at the crack tip (Y. Zhang and Buscarnera 2018).  
552 This effect induces a larger compaction and thus a stronger velocity-weakening behavior. It can  
553 explain the decrease of  $(a-b)$  for the intact gouge for the wet compared to the dry experiments

554 but not the results for the samples submitted to dissolution (in terms of difference wet versus  
555 dry). Indeed, carbonate gouges can present a non-self-similar cataclasis and grain crushing is not  
556 inhibited when reaching a fractal distribution with fractal number 2.6 and they can exhibit higher  
557 fractal numbers than 2.6 (Storti, Billi, and Salvini 2003) compared to silica gouges. Also, the wet  
558 intact sample is the only one of the wet experiments showing a small increase of  $(a-b)$  with the  
559 normal stress, and therefore increasing displacements, for the two velocity steps (Figure 7),  
560 which can also be an effect of the grain crushing as the compaction rate decreases with  
561 increasing displacements. It should be noted that the effects of water like pressure solution or  
562 grain crushing would affect the microstructure of the gouge and therefore the microstructure  
563 would not be the same in the dry and wet samples after the initial shear of the material when the  
564 velocity steps take place.

565 A third mechanism due to the presence of water is the intergranular lubrication, which decreases  
566 intergranular friction and/or adhesion (Cornelio and Violay 2020). This phenomenon leads to a  
567 decrease of friction coefficient and an evolution of  $(a-b)$  towards neutral velocity dependence in  
568 the presence of water compared to the dry case as the effect of changing porosity and thus  
569 contact area is less pronounced inducing in this way less velocity weakening (B. A. Verberne et  
570 al. 2014). These two effects have been observed for the samples with 25% mass dissolution (see  
571 Table 3 and Figure 9). The intergranular lubrication could be dominant in this case due to the  
572 narrower particle size distribution and longer force chains becoming more unstable with the  
573 lubrication. Moreover, it can explain the lower friction coefficient at peak for the wet samples  
574 compared to the dry ones.

575 Therefore, the above considerations seem to indicate that the frictional behavior of our samples  
576 in the presence of water appears to be more controlled by grain breakage/abrasion and pressure  
577 solution (for the value of the friction coefficient at steady state) for the intact gouge, and to  
578 intergranular lubrication for the degraded gouge (25%). The behavior of the gouge with 10%  
579 dissolution is not much affected by the presence of water and it is probably a result of the  
580 different mechanisms described above competing and counteracting each other. The importance  
581 of these mechanisms is inferred to be a result of the narrower particle size distribution and not  
582 the change of grains' roughness induced by dissolution. They lead to an increase of the rate and  
583 state parameter  $(a-b)$  with dissolution for wet gouges, which would decrease the seismic  
584 potential of a fault (that are most of the time saturated) by decreasing the critical stiffness under

585 which it is unstable (eq. 5). Nonetheless, this complex set of microphysical mechanisms  
586 controlling frictional sliding in wet calcite gouges needs to be better constrained using  
587 microphysical observations to evaluate the particle size distribution evolution at different stages  
588 of the experiments and evidences of the mechanisms operating at the interface between the  
589 grains. It will be the subject of future studies.

#### 590 **4.4.Implications for fault reactivation**

591 Our results can have important implications for the study of CO<sub>2</sub> storage or acid gas injection  
592 projects, but also to understand the mechanisms of carbonate bearing faults. Indeed, a great  
593 number of earthquakes are triggered in such lithologies. Noteworthy examples of seismic slips  
594 triggered and propagated through a fault composed of calcite are the magnitude 7.9 Wenchuan  
595 (China) earthquake in 2008 (Chen et al. 2013), the magnitude 6.2 Aigion (Greece) earthquake in  
596 1995 (Bernard et al. 1997), or the magnitude 7.6 Chi-Chi (China) earthquake in 1999 (Boullier et  
597 al. 2009). Carbonate rocks are particularly ubiquitous in Italy and in the Apennines where the  
598 tectonic activity produce number of seismic events, like in the Amatrice and Norcia areas for the  
599 2016-17 seismic sequence (Pizzi et al. 2017), or in L'Aquila for the 2009 earthquake (Valoroso  
600 et al. 2014). Moreover, many reservoirs in the world and potential sites for injection of CO<sub>2</sub>  
601 storage or acid gas disposal are composed or carbonate materials (Bjorlykke 2010) and present  
602 faults that may induce leakage from the storage if they would be reactivated.

603 Sliding along an existing fault favors grain comminution and abrasion and thus, an increase of  
604 the fractal number (Storti, Billi, and Salvini 2003). Our results show that this increase of the  
605 fractal number would tend to destabilize the gouge as faults in the crust are located in a wet  
606 environment. On the other side, injection of an acid fluid tends to decrease this fractal number by  
607 dissolving the small grains. This dissolution decreases the peak friction and promote reactivation  
608 but also would reduce the velocity weakening of the fault and could prevent unstable (seismic)  
609 slips.

610 In our experiments, the maximum amount of mass decrease due to dissolution of calcite that we  
611 have considered is 25%. This high percentage of dissolved mass has been chosen to investigate  
612 whether and how dissolution can affect the frictional properties of fault gouges and a lower  
613 amount of dissolution would be expected in injection projects. However, (Bakker 2017) have  
614 obtained a 25% decrease of calcite content for a carbonate gouge after 10,000 years of CO<sub>2</sub>

615 injection based on geochemical simulations of the long term effect of CO<sub>2</sub> on the mineral  
616 composition of a fault gouge, considering a residence time of 1000 years. In this study, the  
617 authors considered a carbonate bearing claystone and have investigated the effect of long-term  
618 exposure to CO<sub>2</sub> on the frictional properties of the fault by changing its mineral composition  
619 according to the geochemical model and different scenarios. Therefore, the high percentages of  
620 dissolution used in this study could potentially be reached after a long-term injection.

621 However, the experiments presented here have been performed at low normal stresses compared  
622 to the stresses applied to faults at seismogenic depths or typical depths of potential CO<sub>2</sub> storage  
623 sites, which are between at least 800 meters and 5 kilometers depth (Nakanishi et al. 2009), and  
624 acid gas injection sites, which are between 700 meters and 5 kilometers depth (Bachu and Gunter  
625 2002). This would result in normal stresses between 10 and 100 MPa at the fault and also higher  
626 temperatures. The same mechanisms described above are expected to take place at the shallower  
627 depths of the faults at these sites (below 50 MPa (Carpenter et al. 2016)), but their relative  
628 importance would change. Pressure solution and grain crushing becomes both more important  
629 with larger depths and they would have opposite effects on the rate and state parameter (*a-b*) (an  
630 increase for pressure solution and a decrease for grain crushing). On the other side, the viscosity  
631 of supercritical CO<sub>2</sub> is one tenth the one of water, which would affect grain lubrication and tend  
632 to increase (*a-b*) (Cornelio and Violay 2020). At higher depths, crystal plastic deformation could  
633 be triggered and would result in a semi-brittle behavior (Carpenter et al. 2016). Further  
634 investigations would be required using an apparatus that allows to apply higher normal stresses  
635 to the sample in order to further describe the influence of the different mechanisms at larger  
636 depths.

## 637 **5. Concluding remarks**

638 In this paper, we investigate the effect of the injection of an acid fluid on the frictional properties  
639 of a fault located in a carbonate reservoir. The rate and state parameter (*a-b*) of a simulated  
640 calcite gouge are evaluated using an annular shear apparatus and conducting velocity stepping  
641 experiments. The material is dissolved using a strong acid prior to mechanical tests in order to  
642 investigate the potential effect of weak acids in the long-term. We observe that the long-term  
643 exposure to an acid fluid can induce a decrease in the apparent friction and an increase in the rate  
644 and state parameter (*a-b*) for a wet fault by dissolving the small particles and changing the fractal

645 number of the grain size distribution, whereas dry experiments exhibit a decrease of parameter  
646 ( $a-b$ ) with dissolution. Our mechanical results are consistent with an interpretation that the  
647 frictional behavior of dry samples is controlled by grain breakage, which leads to a velocity  
648 weakening when the particles have been exposed to an acid. The presence of water induces  
649 different competing mechanisms: it promotes grain breakage and triggers pressure-solution and  
650 intergranular lubrication. Here, it is suggested that the dissolution of the grains causes a  
651 transition for the frictional behavior to be controlled by grain breakage and pressure-solution to a  
652 behavior more influenced by intergranular lubrication. However, the physical processes driving  
653 the shear behavior of the granular samples need to be further investigated and constrained from  
654 microstructural observations, which will be the focus of future studies. Finally, these  
655 experiments enable us to estimate that chemical reactions could potentially induce the  
656 reactivation of faults by modifying the grain size distribution and, thus, decreasing the apparent  
657 friction but also prevent seismic slip in a storage site by increasing the rate and state parameter  
658 ( $a-b$ ) of the fault. However, this tendency needs to be confirmed by experiments performed with  
659 larger normal stress corresponding to the depths of injection.

660

## 661 **Acknowledgments**

662 This work was supported by the French National Research Agency (ANR FISIC n° ANR-11-  
663 SEED-0003) and the Southern California Earthquake Center (SCEC), award number 118062196.  
664 SCEC is funded by NSF Cooperative Agreement EAR-1033462 and USGS Cooperative  
665 Agreement G12AC20038.

## 666 **References**

- 667 Alevizos, S., Thomas Poulet, and Manolis Veveakis. 2014. “Thermo-Poro-Mechanics of  
668 Chemically Active Creeping Faults. 1: Theory and Steady State Considerations.” *Journal of*  
669 *Geophysical Research: Solid Earth*, June, n/a-n/a. <https://doi.org/10.1002/2013JB010070>.
- 670 An, Lin Ji, and Charles G. Sammis. 1994. “Particle Size Distribution of Cataclastic Fault  
671 Materials from Southern California: A 3-D Study.” *Pure and Applied Geophysics*  
672 *PAGEOPH* 143 (1–3): 203–27. <https://doi.org/10.1007/BF00874329>.
- 673 Anthony, Jennifer L., and Chris J. Marone. 2005. “Influence of Particle Characteristics on  
674 Granular Friction.” *Journal of Geophysical Research B: Solid Earth* 110 (8): 1–14.  
675 <https://doi.org/10.1029/2004JB003399>.

- 676 Atkinson, Barry Kean. 1982. "Subcritical Crack Propagation in Rocks: Theory, Experimental  
677 Results and Applications." *Journal of Structural Geology* 4 (1): 41–56.  
678 [https://doi.org/10.1016/0191-8141\(82\)90005-0](https://doi.org/10.1016/0191-8141(82)90005-0).
- 679 Bachu, Stefan, and William D. Gunter. 2002. "Characteristics of Acid Gas Injection Operations  
680 in Western Canada. Interim Report to International Energy Agency - Greenhouse Gas R&D  
681 Programme."
- 682 ———. 2004. "Acid-Gas Injection in the Alberta Basin, Canada: A CO<sub>2</sub>-Storage Experience." In  
683 *Geological Storage of Carbon Dioxid*, edited by R. H. BAINES, S. J. & WORDEN, 225–  
684 34. Geological Society, London, Special Publications.
- 685 Baisch, Stefan, Robert Vörös, Elmar Rothert, Henrik Stang, Reinhard Jung, and Rüdiger  
686 Schellschmidt. 2010. "A Numerical Model for Fluid Injection Induced Seismicity at Soultz-  
687 Sous-Forets." *International Journal of Rock Mechanics and Mining Sciences* 47: 405–13.  
688 <https://doi.org/10.1016/j.ijrmms.2009.10.001>.
- 689 Bakker, Elisenda. 2017. "Frictional and Transport Properties of Simulated Faults in CO<sub>2</sub> Storage  
690 Reservoirs and Clay-Rich Caprocks." *Utrecht Series in Earth Sciences No124*.
- 691 Beeler, N. M., T. E. Tullis, M. L. Blanpied, and J. D. Weeks. 1996. "Frictional Behavior of  
692 Large Displacement Experimental Faults." *Journal of Geophysical Research B: Solid Earth*  
693 101 (4): 8697–8715. <https://doi.org/10.1029/96jb00411>.
- 694 Bernard, P, P Briole, B Meyer, H Lyon-Caen, J-M Gomez, C Tiberi, C Berge, et al. 1997. "The  
695 Ms=6.2, June 15, 1995 Aigion Earthquake (Greece): Evidence for Low Angle Normal  
696 Faulting in the Corinth Rift." *Journal of Seismology* 1 (2): 131–50.
- 697 Biegel, Ronald L., Charles G. Sammis, and James H. Dieterich. 1989. "The Frictional Properties  
698 of a Simulated Gouge Having a Fractal Particle Distribution." *Journal of Structural  
699 Geology* 11 (7): 827–46. [https://doi.org/10.1016/0191-8141\(89\)90101-6](https://doi.org/10.1016/0191-8141(89)90101-6).
- 700 Billi, Andrea. 2005. "Grain Size Distribution and Thickness of Breccia and Gouge Zones from  
701 Thin (<1 m) Strike-Slip Fault Cores in Limestone." *Journal of Structural Geology* 27 (10):  
702 1823–37. <https://doi.org/10.1016/j.jsg.2005.05.013>.
- 703 Bjorlykke, Knut. 2010. *Petroleum Geoscience: From Sedimentary Enviroments to Rock Physics*.  
704 *Petroleum Geoscience*. <https://doi.org/10.1007/978-3-642-02332-3>.
- 705 Blanpied, Michael L., David A. Lockner, and James D. Byerlee. 1995. "Frictional Slip of Granite  
706 at Hydrothermal Conditions." *Journal of Geophysical Research* 100 (B7): 13045–64.  
707 <https://doi.org/10.1029/95JB00862>.
- 708 Bos, B, C J Peach, and C J Spiers. 2000. "Frictional-Viscous Flow of Simulated Fault Gouge  
709 Caused by the Combined Effects of Phyllosilicates and Pressure Solution." *Tectonophysics*  
710 327: 173–74.
- 711 Boullier, Anne Marie, En Chao Yeh, Sébastien Boutareaud, Sheng Rong Song, and Chin Ho

- 712 Tsai. 2009. “Microscale Anatomy of the 1999 Chi-Chi Earthquake Fault Zone.”  
713 *Geochemistry, Geophysics, Geosystems* 10 (3). <https://doi.org/10.1029/2008GC002252>.
- 714 Brunauer, Stephen, P. H. Emmett, and Edward Teller. 1938. “Adsorption of Gases in  
715 Multimolecular Layers.” *Journal of the American Chemical Society* 60 (2): 309–19.  
716 <https://doi.org/citeulike-article-id:4074706>.
- 717 Cappa, Frederic. 2012. “Impact of CO<sub>2</sub> Geological Sequestration on the Nucleation of  
718 Earthquakes.” *Geophysical Research Letters*, 38, L17313, 2011, September.  
719 <http://escholarship.org/uc/item/15f9x6mp#page-12>.
- 720 Carpenter, B M, C Collettini, C Viti, and A Cavallo. 2016. “The Influence of Normal Stress and  
721 Sliding Velocity on the Frictional Behaviour of Calcite at Room Temperature: Insights from  
722 Laboratory Experiments and Microstructural Observations.” *Geophysical Journal  
723 International* 205 (1): 548–61. <https://doi.org/10.1093/gji/ggw038>.
- 724 Chambon, G., J. Schmittbuhl, A. Corfdir, J. P. Vilotte, and S. Roux. 2003. “Shear with  
725 Comminution of a Granular Material: Microscopic Deformations Outside the Shear Band.”  
726 *Physical Review E - Statistical Physics, Plasmas, Fluids, and Related Interdisciplinary  
727 Topics* 68 (1): 8. <https://doi.org/10.1103/PhysRevE.68.011304>.
- 728 Chambon, Guillaume. 2003. “Caractérisation Expérimentale Du Frottement Effectif Des Zones  
729 de Faille.” École Nationale des Ponts et Chaussées. [http://tel.archives-ouvertes.fr/tel-  
730 00006613/](http://tel.archives-ouvertes.fr/tel-00006613/).
- 731 Chambon, Guillaume, Jean Schmittbuhl, and Alain Corfdir. 2006a. “Frictional Response of a  
732 Thick Gouge Sample: 1. Mechanical Measurements and Microstructures.” *Journal of  
733 Geophysical Research: Solid Earth* 111 (9): 1–17. <https://doi.org/10.1029/2003JB002731>.
- 734 ———. 2006b. “Frictional Response of a Thick Gouge Sample: 2. Friction Law and  
735 Implications for Faults.” *Journal of Geophysical Research: Solid Earth* 111 (9): 1–12.  
736 <https://doi.org/10.1029/2004JB003339>.
- 737 Chen, Jianye, Xiaosong Yang, Shengli Ma, and Christopher J Spiers. 2013. “Mass Removal and  
738 Clay Mineral Dehydration/Rehydration in Carbonate-Rich Surface Exposures of the 2008  
739 Wenchuan Earthquake Fault: Geochemical Evidence and Implications for Fault Zone  
740 Evolution and Coseismic Slip.” *Journal of Geophysical Research: Solid Earth* 118 (2):  
741 474–96. <https://doi.org/10.1002/jgrb.50089>.
- 742 Coop, M. R., K. K. Sorensen, T. Bodas Freitas, and G. Georgoutsos. 2004. “Particle Breakage  
743 during Shearing of a Carbonate Sand.” *Geotechnique* 54 (3): 157–63.  
744 <https://doi.org/10.1680/geot.2004.54.3.157>.
- 745 Corfdir, Alain, Patrick Lerat, and Ioannis Vardoulakis. 2004. “A Cylinder Shear Apparatus.”  
746 *Geotechnical Testing Journal* 27 (5): 447–55. <https://doi.org/10.1520/gtj11551>.
- 747 Cornelio, Chiara, and Marie Violay. 2020. “Effect of Fluid Viscosity on Earthquake Nucleation.”  
748 *Geophysical Research Letters* 47: 1–9. <https://doi.org/10.1029/2020GL087854>.

- 749 Das, Soukat Kumar, and Arghya Das. 2019. "Influence of Quasi-Static Loading Rates on  
750 Crushable Granular Materials: A DEM Analysis." *Powder Technology* 344 (January 2019):  
751 393–403. <https://doi.org/10.1016/j.powtec.2018.12.024>.
- 752 Dieterich, James H. 1979. "Modeling of Rock Friction: 1. Experimental Results and Constitutive  
753 Equations." *Journal of Geophysical Research* 84 (B5): 2161.  
754 <https://doi.org/10.1029/JB084iB05p02161>.
- 755 ———. 1981. "Constitutive Properties of Faults with Simulated Gouge." *Geophysical*  
756 *Monograph Series* 24: 103–20.  
757 <http://www.agu.org/books/gm/v024/GM024p0103/GM024p0103.shtml>.
- 758 Ellsworth, William L. 2013. "Injection-Induced Earthquakes." *Science* 341 (July): 1–8.
- 759 Ende, M. P.A. van den, J. Chen, J. P. Ampuero, and A. R. Niemeijer. 2018. "A Comparison  
760 between Rate-and-State Friction and Microphysical Models, Based on Numerical  
761 Simulations of Fault Slip." *Tectonophysics* 733 (July 2017): 273–95.  
762 <https://doi.org/10.1016/j.tecto.2017.11.040>.
- 763 Espinoza, D Nicolas. 2011. "Carbon Geological Storage – Underlying Phenomena and  
764 Implications –."
- 765 Foulger, Gillian R, Miles P Wilson, Jon G Gluyas, Bruce R Julian, and Richard J Davies. 2018.  
766 "Global Review of Human-Induced Earthquakes." *Earth-Science Reviews* 178 (July 2017):  
767 438–514. <https://doi.org/10.1016/j.earscirev.2017.07.008>.
- 768 Han, Raehee, Toshihiko Shimamoto, T Hirose, J H Ree, and J Ando. 2007. "Ultralow Friction of  
769 Carbonate Faults Caused by Thermal Decomposition." *Science* 316 (5826): 878–81.  
770 <https://doi.org/10.1126/science.1139763>.
- 771 Karimpour, Hamid, and Poul V. Lade. 2010. "Time Effects Relate to Crushing in Sand." *Journal*  
772 *of Geotechnical and Geoenvironmental Engineering* 136 (9): 1209–19.  
773 [https://doi.org/10.1061/\(ASCE\)GT.1943-5606.0000335](https://doi.org/10.1061/(ASCE)GT.1943-5606.0000335).
- 774 Khan, Chawarwan, Robert Amin, and Gary Madden. 2013. "Effects of CO<sub>2</sub> and Acid Gas  
775 Injection on Enhanced Gas Recovery and Storage." *Journal of Petroleum Exploration and*  
776 *Production Technology* 3 (1): 55–60. <https://doi.org/10.1007/s13202-012-0044-8>.
- 777 Kirk-Othmer. 2004. *Kirk-Othmer Encyclopedia of Chemical Technology, Volume 4*. Edited by  
778 Kirk-Othmer. 2004th ed. Hoboken, NJ: Wiley.
- 779 Koval, Georg, François Chevoir, Jean-Noël Roux, Jean Sulem, and Alain Corfdir. 2011.  
780 "Interface Roughness Effect on Slow Cyclic Annular Shear of Granular Materials."  
781 *Granular Matter* 13 (5): 525–40. <https://doi.org/10.1007/s10035-011-0267-2>.
- 782 Lund, Kasper, H. S. Fogler, C. C. McCune, and J. W. Ault. 1975. "Acidization-II. The  
783 Dissolution of Calcite in Hydrochloric Acid." *Chemical Engineering Science* 30 (8): 825–  
784 35. [https://doi.org/10.1016/0009-2509\(75\)80047-9](https://doi.org/10.1016/0009-2509(75)80047-9).

- 785 Mair, Karen, and James F. Hazzard. 2007. "Nature of Stress Accommodation in Sheared  
786 Granular Material: Insights from 3D Numerical Modeling." *Earth and Planetary Science*  
787 *Letters* 259 (3–4): 469–85. <https://doi.org/10.1016/j.epsl.2007.05.006>.
- 788 Marone, Chris J. 1998. "Laboratory-Derived Friction Laws and Their Application To Seismic  
789 Faulting." *Annual Review of Earth and Planetary Sciences* 26 (1): 643–96.  
790 <https://doi.org/10.1146/annurev.earth.26.1.643>.
- 791 Messen, Y. H., A. Corfdir, and J. Schmittbuhl. 2013. "Mechanical Healing of Simulated Fault  
792 Gouge." *Geophysical Journal International* 193 (1): 252–62.  
793 <https://doi.org/10.1093/gji/ggs082>.
- 794 Michael, K., A. Golab, V. Shulakova, J. Ennis-King, G. Allinson, S. Sharma, and T. Aiken.  
795 2010. "Geological Storage of CO<sub>2</sub> in Saline Aquifers-A Review of the Experience from  
796 Existing Storage Operations." *International Journal of Greenhouse Gas Control* 4 (4): 659–  
797 67. <https://doi.org/10.1016/j.ijggc.2009.12.011>.
- 798 Micić, Vesna, Doris Schmid, Nathan Bossa, Andreas Gondikas, Milica Velimirovic, Frank Von  
799 Der Kammer, Mark R. Wiesner, and Thilo Hofmann. 2017. "Impact of Sodium Humate  
800 Coating on Collector Surfaces on Deposition of Polymer-Coated Nanoiron Particles."  
801 *Environmental Science and Technology* 51 (16): 9202–9.  
802 <https://doi.org/10.1021/acs.est.7b01224>.
- 803 Mortezaei, Kimia, and Farshid Vahedifard. 2015. "Numerical Simulation of Induced Seismicity  
804 in Carbon Capture and Storage Projects." *Geotechnical and Geological Engineering* 33 (2):  
805 411–24. <https://doi.org/10.1007/s10706-015-9859-7>.
- 806 Nakanishi, Shigetaka, Yasunobu Mizuno, Tadahiko Okumura, Hideaki Miida, Takumi  
807 Shidahara, and Shin-ichi Hiramatsu. 2009. "Methodology of CO<sub>2</sub> Aquifer Storage Capacity  
808 Assessment in Japan and Overview of the Project." *Energy Procedia* 1 (1): 2639–46.  
809 <https://doi.org/10.1016/j.egypro.2009.02.031>.
- 810 Niemeijer, André, Derek Elsworth, and Chris Marone. 2009. "Significant Effect of Grain Size  
811 Distribution on Compaction Rates in Granular Aggregates." *Earth and Planetary Science*  
812 *Letters* 284 (3–4): 386–91. <https://doi.org/10.1016/j.epsl.2009.04.041>.
- 813 Ovalle, C., C. Voivret, C. Dano, and P.-Y. Hicher. 2016. "Population Balance in Confined  
814 Comminution Using a Physically Based Probabilistic Approach for Polydisperse Granular  
815 Materials." *International Journal for Numerical and Analytical Methods in Geomechanics*  
816 40: 2383–2397. <https://doi.org/10.1002/nag>.
- 817 Ovalle, Carlos, Christophe Dano, Pierre Yves Hicher, and Mónica Cisternas. 2015.  
818 "Experimental Framework for Evaluating the Mechanical Behavior of Dry and Wet  
819 Crushable Granular Materials Based on the Particle Breakage Ratio." *Canadian*  
820 *Geotechnical Journal* 52 (5): 587–98. <https://doi.org/10.1139/cgj-2014-0079>.
- 821 Pizzi, A., A. Di Domenica, F. Gallovic, L. Luzi, and R. Puglia. 2017. "Fault Segmentation as  
822 Constraint to the Occurrence of the Main Shocks of the 2016 Central Italy Seismic

- 823 Sequence.” *Tectonics* 36 (11): 2370–87. <https://doi.org/10.1002/2017TC004652>.
- 824 Pluymakers, A. M.H., A. R. Niemeijer, and C. J. Spiers. 2016a. “Frictional Properties of  
825 Simulated Anhydrite-Dolomite Fault Gouge and Implications for Seismogenic Potential.”  
826 *Journal of Structural Geology* 84: 31–46. <https://doi.org/10.1016/j.jsg.2015.11.008>.
- 827 ———. 2016b. “Frictional Properties of Simulated Anhydrite-Dolomite Fault Gouge and  
828 Implications for Seismogenic Potential.” *Journal of Structural Geology*.  
829 <https://doi.org/10.1016/j.jsg.2015.11.008>.
- 830 Pluymakers, Anne M H, Jon E Samuelson, André R Niemeijer, and Christopher J Spiers. 2014.  
831 “Effects of Temperature and CO2 on the Frictional Behavior of Simulated Anhydrite Fault  
832 Rock.” *Journal of Geophysical Research: Solid Earth* 119,: 8728–8747.  
833 <https://doi.org/10.1002/2014JB011575>.Received.
- 834 Rattez, Hadrien, Ioannis Stefanou, and Jean Sulem. 2018. “The Importance of Thermo-Hydro-  
835 Mechanical Couplings and Microstructure to Strain Localization in 3D Continua with  
836 Application to Seismic Faults. Part I: Theory and Linear Stability Analysis.” *Journal of the  
837 Mechanics and Physics of Solids* 115: 54–76. <https://doi.org/10.1016/j.jmps.2018.03.004>.
- 838 Rattez, Hadrien, Ioannis Stefanou, Jean Sulem, Manolis Veveakis, and Thomas Poulet. 2018.  
839 “The Importance of Thermo-Hydro-Mechanical Couplings and Microstructure to Strain  
840 Localization in 3D Continua with Application to Seismic Faults . Part II: Numerical  
841 Implementation and Post-Bifurcation Analysis.” *Journal of the Mechanics and Physics of  
842 Solids* 115: 1–29. <https://doi.org/10.1016/j.jmps.2018.03.003>.
- 843 Rattez, Hadrien, Ioannis Stefanou, Manolis Veveakis, Thomas Poulet, and Jean Sulem. 2018.  
844 “Numerical Analysis of Strain Localization in Rocks with THM Couplings: Benchmark  
845 Tests and Microstructure.” *Rock Mechanics and Rock Engineering*.
- 846 Rattez, Hadrien, Jean Sulem, and Siavash Ghabezloo. 2014. “Effect of CO2 on Fault Friction  
847 and Slip Stability.” In *25th ALERT Workshop, Aussois, France*.
- 848 Rattez, Hadrien, and Manolis Veveakis. 2020. “Weak Phases Production and Heat Generation  
849 Control Fault Friction during Seismic Slip.” *Nature Communications* 11 (350).  
850 <https://doi.org/10.1038/s41467-019-14252-5>.
- 851 Reid, Harry F. 1910. “The Mechanism of the Earthquake.” In *The California Earthquake of April  
852 18, 1906, Report of the State Earthquake Investigation Commision, Vol. 2*, 1–192.
- 853 Rice, James R. 2006. “Heating and Weakening of Faults during Earthquake Slip.” *Journal of  
854 Geophysical Research: Solid Earth* 111 (5). <https://doi.org/10.1029/2005JB004006>.
- 855 Rice, James R., and A Ruina. 1983. “Stability of Steady Frictional Slipping.” *Journal of Applied  
856 Mechanics* 50 (2): 343. <https://doi.org/10.1115/1.3167042>.
- 857 Rohmer, J., A. Pluymakers, and F. Renard. 2016. “Mechano-Chemical Interactions in  
858 Sedimentary Rocks in the Context of CO2 Storage: Weak Acid, Weak Effects?” *Earth-*

- 859 *Science Reviews* 157 (June 2016): 86–110. <https://doi.org/10.1016/j.earscorev.2016.03.009>.
- 860 Rubinstein, Justin L., and Alireza Babaie Mahani. 2015. “Myths and Facts on Wastewater  
861 Injection, Hydraulic Fracturing, Enhanced Oil Recovery, and Induced Seismicity.”  
862 *Seismological Research Letters* 86 (4): 1060–67. <https://doi.org/10.1785/0220150067>.
- 863 Ruina, A. 1983. “Slip Instability and State Variable Friction Laws.” *Journal of Geophysical*  
864 *Research: Solid Earth* 88 (12): 10,359–10,370.  
865 <http://onlinelibrary.wiley.com/doi/10.1029/JB088iB12p10359/full>.
- 866 Sammis, Charles G., Geoffrey King, and Ronald L. Biegel. 1987. “The Kinematics of Gouge  
867 Deformation.” *Pure and Applied Geophysics* 125 (5): 777–812.  
868 <https://doi.org/10.1007/BF00878033>.
- 869 Samuelson, Jon E, and Christopher J Spiers. 2012. “Fault Friction and Slip Stability Not  
870 Affected by CO2 Storage : Evidence from Short-Term Laboratory Experiments on North  
871 Sea Reservoir Sandstones and Caprocks.” *International Journal of Greenhouse Gas Control*  
872 Volume 11 (November 2012): 78–90.
- 873 Schoenball, Martin, and William Ellsworth. 2017. “A Systematic Assessment of the  
874 Spatiotemporal Evolution of Fault Activation Through Induced Seismicity in Oklahoma and  
875 Southern Kansas.” *Journal of Geophysical Research : Solid Earth* 122 (12): 10,189–10,206.  
876 <https://doi.org/10.1002/2017JB014850>.
- 877 Scholz, Christopher H. 1998. “Earthquakes and Friction Laws.” *Nature* 391 (January 1998): 37–  
878 42.
- 879 Scuderi, Marco M., André R Niemeijer, Cristiano Collettini, and Chris J. Marone. 2013.  
880 “Frictional Properties and Slip Stability of Active Faults within Carbonate–Evaporite  
881 Sequences: The Role of Dolomite and Anhydrite.” *Earth and Planetary Science Letters*  
882 369–370 (May): 220–32. <https://doi.org/10.1016/j.epsl.2013.03.024>.
- 883 Smith, Steven A. F., Stefan Nielsen, and Giulio Di Toro. 2015. “Strain Localization and the  
884 Onset of Dynamic Weakening in Calcite Fault Gouge.” *Earth and Planetary Science Letters*  
885 413 (March): 25–36. <https://doi.org/10.1016/j.epsl.2014.12.043>.
- 886 Steacy, S J, and C G Sammis. 1991. “An Automaton for Fractal Patterns of Fragmentation.”  
887 *Nature* 353 (6341): 250–52. <https://doi.org/10.1038/353250a0>.
- 888 Storti, Fabrizio, Andrea Billi, and Francesco Salvini. 2003. “Particle Size Distributions in  
889 Natural Carbonate Fault Rocks : Insights for Non-Self-Similar Cataclasis.” *Earth and*  
890 *Planetary Science Letters* 206: 173–86.
- 891 Sulem, Jean, and V Famin. 2009. “Thermal Decomposition of Carbonates in Fault Zones: Slip-  
892 Weakening and Temperature-Limiting Effects.” *Journal of Geophysical Research* 114 (B3):  
893 1–14. <https://doi.org/10.1029/2008JB006004>.
- 894 Tembe, Sheryl, David A. Lockner, and Teng Fong Wong. 2010. “Effect of Clay Content and

- 895 Mineralogy on Frictional Sliding Behavior of Simulated Gouges: Binary and Ternary  
896 Mixtures of Quartz, Illite, and Montmorillonite.” *Journal of Geophysical Research: Solid*  
897 *Earth* 115 (3): 1–22. <https://doi.org/10.1029/2009JB006383>.
- 898 Torabi, A., M. U. Johannessen, and T. S. S. Ellingsen. 2019. “Fault Core Thickness: Insights  
899 from Siliciclastic and Carbonate Rocks.” *Geofluids* 2019: 1–24.  
900 <https://doi.org/10.1155/2019/2918673>.
- 901 Unterreiner, P., P. Lerat, I. Vardoulakis, F. Schlosser, E. De Laure, and G. Belmont. 1993.  
902 Brevet sur l’Appareil de Cisaillement Simple Annulaire (ACSA), issued 1993.
- 903 Valoroso, Luisa, Lauro Chiaraluce, Cristiano Collettini, Istituto Nazionale, Vigna Murata,  
904 Dipartimento Scienze, Sapienza Università, and Piazzale Aldo Moro. 2014. “Earthquakes  
905 and Fault Zone Structure.” *Geology* 42 (4): 343–46. <https://doi.org/10.1130/G35071.1>.
- 906 Verberne, B. a., Christopher J Spiers, a. R. Niemeijer, J. H. P. Bresser, D. a. M. Winter, and O.  
907 Plümper. 2013. “Frictional Properties and Microstructure of Calcite-Rich Fault Gouges  
908 Sheared at Sub-Seismic Sliding Velocities.” *Pure and Applied Geophysics*, December.  
909 <https://doi.org/10.1007/s00024-013-0760-0>.
- 910 Verberne, B. A., Christopher J Spiers, André R Niemeijer, J. H P De Bresser, D. A M De Winter,  
911 and O. Plümper. 2014. “Frictional Properties and Microstructure of Calcite-Rich Fault  
912 Gouges Sheared at Sub-Seismic Sliding Velocities.” *Pure and Applied Geophysics* 171  
913 (10): 2617–40. <https://doi.org/10.1007/s00024-013-0760-0>.
- 914 Verberne, Berend A., André R. Niemeijer, Johannes H.P. De Bresser, and Christopher J. Spiers.  
915 2015. “Mechanical Behavior and Microstructure of Simulated Calcite Fault Gouge Sheared  
916 at 20–600°C: Implications for Natural Faults in Limestones.” *Journal of Geophysical*  
917 *Research: Solid Earth* 120: 8169–96. <https://doi.org/10.1002/2015JB012292>.Received.
- 918 Veveakis, Manolis, Thomas Poulet, and S. Alevizos. 2014. “Thermo-Poro-Mechanics of  
919 Chemically Active Creeping Faults: 2. Transient Considerations.” *Journal of Geophysical*  
920 *Research: Solid Earth* 119 (6): 4583–4605. <https://doi.org/10.1002/2013JB010071>.
- 921 Wilson, M. P., G. R. Foulger, J. G. Gluyas, R. J. Davies, and B. R. Julian. 2017. “*HiQuake* : The  
922 Human- Induced Earthquake Database.” *Seismological Research Letters* 88 (6): 1560–65.  
923 <https://doi.org/10.1785/0220170112>.
- 924 Yehya, Alissar, Zhuo Yang, and James Robert Rice. 2018. “Effect of Fault Architecture and  
925 Permeability Evolution on Response to Fluid Injection.” *Journal of Geophysical Research:*  
926 *Solid Earth* 123 (11): 9982–97. <https://doi.org/10.1029/2018JB016550>.
- 927 Zhang, X., and C. J. Spiers. 2005. “Compaction of Granular Calcite by Pressure Solution at  
928 Room Temperature and Effects of Pore Fluid Chemistry.” *International Journal of Rock*  
929 *Mechanics and Mining Sciences* 42: 950–60. <https://doi.org/10.1016/j.ijrmms.2005.05.017>.
- 930 Zhang, Y. D., and G. Buscarnera. 2017. “A Rate-Dependent Breakage Model Based on the  
931 Kinetics of Crack Growth at the Grain Scale.” *Géotechnique* 67 (11): 953–67.

932 <https://doi.org/10.1680/jgeot.16.p.181>.

933 Zhang, Yida, and Giuseppe Buscarnera. 2018. "Breakage Mechanics for Granular Materials in  
934 Surface-Reactive Environments." *Journal of the Mechanics and Physics of Solids* 112: 89–  
935 108. <https://doi.org/10.1016/j.jmps.2017.11.008>.

936